Coherence scanning interferometry allows accurate characterization of micrometric spherical particles contained in complex media

Remy Claveau, Paul Montgomery, Manuel Flury

Title: Coherence scanning interferometry allows accurate characterization of micrometric spherical particles contained in complex media

Authors: Rémy Claveau, Paul Montgomery, and Manuel Flury

Affiliations: ICube, Université de Strasbourg, CNRS (UMR 7357), INSA, F-67000 Strasbourg, France

*Corresponding author: mflury@unistra.fr

Abstract: Characterizing very small particles, from a few dozen micrometers to the nanometric scale, is a very challenging application in a wide range of domains. In this work, we demonstrate, through the recovery of silica and polystyrene bead properties (i.e. their size and refractive index) that Coherence Scanning Interferometry (CSI), in addition of being contactless, non-destructive, label-free and very well spatially resolved, is a very interesting and promising tool for such complex characterization. The CSI system is used as an imaging Fourier transform spectrometer meaning that the characterizations are achieved by analyzing the interference signal in the spectral domain. Some simulations of the proposed technique are presented and show that the accuracy of such characterization, in particular the measurement of the refractive index, are closely related to the signal to noise ratio. This observation is thereafter confirmed by the experimental results of beads buried within the depth of a transparent sample. Finally, the method is theoretically tested in the case of a scattering medium in which the quality of the signal is highly degraded. In this context, a geometrical approach enabling the simulation of an interference signal from a scattering layer is first proposed and then validated by means of comparison with experimental data.

Keywords: Interference microscopy, Optical inspection, Fringe analysis, Optical properties, Spectroscopy, Fourier transforms.

1. Introduction

The precise characterization of very small-sized particles has become an important area of research over the last few years, its interest affecting many different domains. As an example, the medical and biological fields require this kind of characterization since the spectral and/or morphological analysis of single organic particles (cells) can be used for detecting various diseases such as cancer [1,2]. In other fields, such as materials and art, the possibility of obtaining the optical and morphological properties of individual structures buried within the depth of a transparent layer is also considerable as it enables the identification and classification of the different samples [3,4]. Consequently, many techniques have been directed towards this research theme with the same final purpose of aiming at rapidity and accuracy in the characterization. In the literature it can be seen that there is a very pronounced use of optical microscopy techniques because of their non-invasive nature, which is essential in the medical and biological fields. Among them, label-based techniques such as fluorescent microscopy allow the easy detection, differentiation and imaging of different kinds of particles depending on

either their fluorescence properties or their associated fluorophores [5,6]. In order to avoid the modification or distortion of the particles studied, unlabelled optical techniques have been brought to the forefront. The literature mainly reveals a strong use of near-field microscopy (SNOM) and hyperspectral microscopy techniques as well as those based on low coherence interferometry (LCI). In the case of near-field microscopy methods, the SNOM configuration allows the diffraction limit to be overcome and is associated with infrared spectroscopy systems. The ability of such setups to characterize very small structures has already been demonstrated. Indeed, this technique, known as IR-SNOM (or nano-FTIR) has been used for identifying the molecular fingerprints of an organic sample at a resolution of 20 nm [7] as well as for mapping and carrying out the structural analysis of individual proteins [8], nanoparticles and viruses [9]. Despite its excellent spatial resolution, IR-SNOM has some significant drawbacks. First, because of the very short working distance of the system (about one hundred nanometers), the measurements are limited to the sample surface, so that performing a depth-resolved study is impossible. In addition, the measurement being local, the characterization of a sample over large areas requires very long scanning times. Other methods, known as hyperspectral microscopy (association of hyperspectral imaging to microscopy techniques) have been developed for providing local spectral measurements and spectroscopic mapping at nanometric spatial resolutions. Two main configurations can be seen in the literature, respectively called hyperspectral darkfield microscopy [10] and hyperspectral reflected light microscopy [11]. Both of these systems work with the same principle and generally use either an imaging spectrometer or a tunable supercontinuum source together with a CCD camera for recording the hyperspectral data cube. Through the spectral measurements allowed by these systems, the detection and characterization of nanoparticles in complex waters have been demonstrated [12] provided they have a low enough density to be distinguished individually, each one having an image size of the Airy spot. This technique has also been widely used for biological purposes as it enables the spatial mapping and spectral characterization of gold and Au/Ag alloy nanoparticles targeting specific human cancer cells [11,13]. Compared to SNOM, hyperspectral microscopy enables imaging within the depth (at different Z planes) but still possesses some limitations. Indeed, this method does not provide the possibility of producing a spectral measurement resolved in the three directions of space, thus preventing any characterization of single particles located at a specific position along Z. Moreover, each 2D image (XY or Xλ image) at one given spectral band (or Y position) is obtained independently, leading to a sequential recording of the data as a function of either the wavelength or Y position. As such, at least one supplementary scanning step is necessary and as soon as the spectral band studied is wider or a very fine spectral resolution is desired, the acquisition time increases. To obtain quantitative information about particles buried within the depth of a transparent sample, recent work based on the association of LCI with Light Scattering Spectroscopy (LSS) has been carried out. Indeed, the technique of LSS is well-known and has already been used in a microscopy system for providing a wealth of information on particles through their elastic light-scattering properties [14]. This simple configuration not being resolved over the depth, the combination with interference microscopy made it possible to overcome this limitation, giving birth to an

original technique known as angle-resolved Low Coherence Interferometry (aLCI) [15]. This technique is intended for the determination of the size of scattering particles. To do so, the information provided by the scattered intensity as a function of the scattering angle is used. Then, the recovery of the particle size is obtained from the comparison between the experimental data and the results predicted by Mie theory [16]. As this technique enables the mapping of the angular scattering as a function of the optical path, the measurement performed is resolved over the depth [17]. However, because of the arrangement of the optical system and the processing applied to the signal, the measurement is no longer resolved laterally. It is therefore not possible to distinguish the spectral responses of the different particles in the case where various kinds of microspheres are located in the same image volume. Indeed, we can note in this work that the characterization of the microspheres is carried out through the analysis of homogeneous samples, i.e. containing a set of scatterers having identical properties (as regards the size and the type of material). This bibliographic study reveals how complicated it is to find a characterization technique being at the same time fast, accurate, 3D-resolved and allowing quantitative information to be obtained. We will show in this paper that coherence scanning interferometry used in its Fourier transform spectrometer (FTS) operating mode [18, 19], is a technique that fulfils nearly all of the previously mentioned criteria and that by using a specific processing of the interference signal, the optical and morphological characterizations of single particles are possible. Fig. 1 illustrates a typical signal measured from a spherical particle buried within a transparent sample. Its very poor signal-to-noise ratio (SNR) highlights how difficult the analysis can be. By working in the spectral domain rather than the spatial domain, the recovery of the particle properties can be achieved by only using data where the SNR is higher than a certain threshold. We will begin by presenting the spectral analysis of interferometric data from which the properties of the particles are extracted.

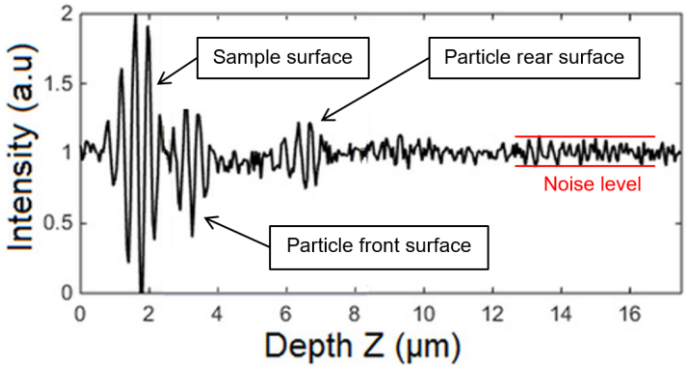

Fig. 1. Typical interference signal acquired from a spherical particle buried within a transparent layer. The refractive index contrast between the particle and the medium is 0.1. In many applications it can be much lower, further complicating the analysis.

2. Theoretical background of spectral measurements in CSI

The method used to optically and morphologically characterize micrometric spherical particles is based on the analysis of their backscattering spectrum, which is obtained from the spectral analysis of the interference signals. As explained later, the principle is based on matching the resulting experimental backscattering

spectrum of the particle with the theoretical one. The knowledge of the theoretical spectral response of such micrometric particles is therefore an essential part of our approach.

A. Acquisition and basic spectral analysis of interferometric data

Coherence scanning interferometry is a measurement method based on the acquisition of an image sequence of interference patterns resulting from the superposition of the light coming back from the sample and the light reflected from a reference mirror (Fig. 2(a)). By looking at the intensity profile along the Z-axis at different pixels in this image stack, multiple interference signals can be extracted to provide information from different points in the sample (Fig. 2(b)). The study, which can be either topographic [20], tomographic [21] or spectral [22], is then always performed through a specific processing of these signals. In the present case, this processing only consists in applying a Fourier transform to the white fringes.

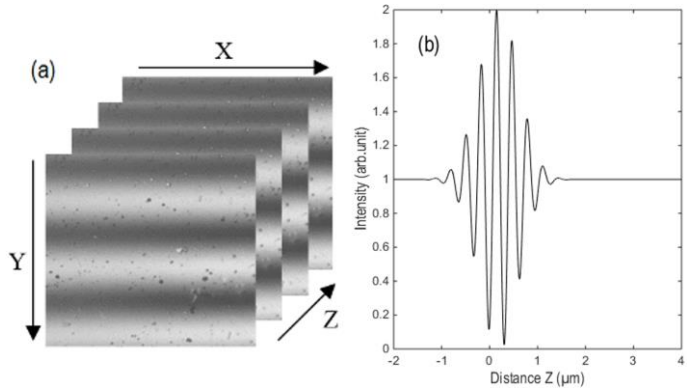

Fig. 2. (a) Interferometric image stack of a silicon sample. (b) Example of a signal extracted from one pixel in this stack

We recall that the classical expression of an interference signal (Fig. 2(b)), assuming its part independent from z is omitted, is given by Eq. 1.

$$I(z) = \int_k \int_\theta \pi S(k) \left| r_{ref} \right| \left| r_s(k,\theta) \right| \cos\left(\Delta\varphi(k,\theta) + \phi\right) d\theta dk \qquad \textbf{(1)}$$

where $S(k)$ is the power spectral density of the source at the wave number k, $\left|r_{ref}\right|$ and $|r_s|$ are the amplitude reflection coefficients of the reference mirror and the sample respectively, θ is the incident angle, $\Delta\varphi = 2kzcos(\theta)$ is the optical path difference between the reference and object arms and ϕ is the phase shift due to the reflection.

It is quite easy to demonstrate that this signal and the spectral transfer function of the system (STF) are related to each other by a Fourier transform operation (Eq. 2). The STF is defined as the product of the illumination source, the reference mirror reflectivity, the detector spectral response and the optical components transmittance. Consequently, following a calibration step intended to determine the STF, we show that the reflectance of the sample R_s, which characterizes the fraction of reflected intensity, is given by Eq. 3 [22, 23].

$$\left|FT\left[I(z)\right]\right| = STF(k)\cdot\left|r_s(k)\right| \qquad (2)$$

$$R_s(k) = \frac{\left|FT\left[I(z)\right]\right|^2}{STF(k)^2} \qquad (3)$$

B. Case of a transparent layer

In the case of a transparent layer, the spectral analysis of the interference signal provides the total reflectance spectrum of the layer (Eq. 4). However, this reflectance spectrum depends on the ratio between the optical thickness of the layer (OT) and the coherence length of the source as shown by Eq. 5 [24].

$$r_{tot}(k) = \left|r_{tot}(k)\right|\cdot e^{jf_{tot}} = \frac{FT\left[I(z)\right]}{STF(k)} \qquad (4)$$

$$\begin{cases} r_{tot}(k) = \dfrac{r_{S_1} + r_{S_2}e^{-j2b}}{1 + r_{S_1}r_{S_2}e^{-j2b}} & \text{if } \dfrac{2OT}{l_{coh}} < 1 \\ r_{tot}(k) = \left|r_{S_1}\right|e^{jf_1} + \left|r_{S_2}\right|\left|t_{S_1}\right|^2 e^{j(f_2 - 2b)} & \text{if } \dfrac{2OT}{l_{coh}} > 1 \end{cases} \qquad (5)$$

The terms $|r_{S_1}|$ and $|r_{S_2}|$ are the magnitude of the Fresnel reflection coefficient of the front and rear interfaces respectively and $|t_{S_1}|$ is the amplitude transmission of the surface. The possible phase shifts due to reflection are introduced by ϕ_1 and ϕ_2. The term β is defined as $\beta = ken\cos\theta'$ with θ' as the propagation angle of the light within the layer and e and n as the thickness and refractive index of the layer.

If twice the optical thickness / coherence length ratio is less than one, the reflectance spectrum is then expressed as the well-known total reflection coefficient that is used to describe the behavior of a thin film structure of several hundred nanometers thick. However, when twice the OT is greater than the coherence length of the source, the light reflected by the front and rear interfaces no longer interfere with each other. In addition, the light that propagates more than one round trip within the layer is neglected because it possesses an optical path much higher than that being reflected only once. These considerations lead to the spectrum expressed in the second part of Eq. 5. In practice, because the transition from complete temporal coherence to complete incoherence is not abrupt, an intermediate case of partial coherence should be considered around $2OT = l_{coh}$ and Eq. 5 mostly refers to limiting cases, i.e. $2OT \ll l_{coh}$ and $2OT \gg l_{coh}$. In the case of complete incoherence, we also showed that it was possible to extract only the depth-resolved reflectance spectrum of the buried interface since the separation of each interferogram is large enough [25]. From this work it was also demonstrated that the spectral analysis of interferometric data within the depth of a sample requires a low numerical aperture.

C. Theoretical response of micrometric spherical particles

As explained before, it is crucial to determine the theoretical spectral behavior of the structure studied. The previous section demonstrated that in our interferometric approach, the spectrum measured is dependent on both the structural features and the coherence length of the source. The response of spherical particles being much more complicated than that of transparent layers, it is essential to well define the theoretical expression of the backscattering spectrum. Firstly, depending on the particle size compared to the wavelength, the scattering will either be described by Mie theory or by the Rayleigh regime. In our case, because we study micrometric spherical particles with a diameter included in the $[\lambda; 10\lambda]$ range, the scattering phenomenon is predicted by Mie theory. However, this theory models the interference between coherent monochromatic light that is reflected from the front and rear surfaces of the spherical particle. Consequently, to apply Mie theory, the optical path length due to one round trip of the light within the particle must not exceed the coherence length of the source. If this condition is not met, the two components cannot interfere, and the spectral analysis of the backscattered signal will lead to a spectrum similar to that defined in the lower equation of Eq. 5. This difference must be taken into account since the backscattering spectra of the same sphere obtained from these two models are significantly different, as shown in Fig. 3.

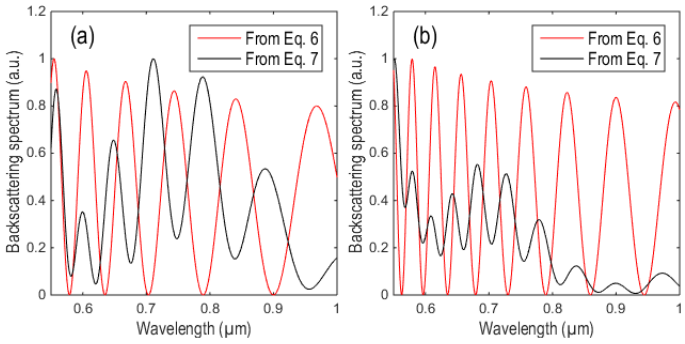

Fig. 3. Backscattering spectra of a polystyrene bead (n = 1.58) contained in a transparent layer (n = 1.4). The radius of the bead is (a) 1 µm (b) 1.5 µm. The black spectra are obtained from Mie theory predictions as the scattering from the front and back surfaces is coherent. The red spectra are obtained from the transparent film model as the difference in optical path is greater than the coherence length of the source.

A polystyrene bead with an average refractive index of 1.58 two different radii is considered and is assumed to be included in a medium with an optical index of 1.4. For these simulations, the bead is assumed to be illuminated by plane waves with incidence directions within a cone of NA = 0.1. The red spectra are obtained from Eq. 6 which is derived from the reflectance model of a transparent layer defined by the lower part of Eq. 5. The only difference is the consideration of the reflection at the interface between the surrounding medium and the layer that contains the sphere, which is introduced by the coefficient r_{01}. Although this model omits some effects occurring in a spherical particle, such as focusing effects due to the curved edges, introducing these in a theoretical model is not simple. For this reason, we decided to use this simplified expression, which, in addition,

can be used more broadly for different kinds of particles and substantially reduces the complexity of the processing for the recovery of the size and refractive index.

$$\left|s_b(k)\right|^2 = \left(1 - r_{01}^2\right)^2 \left[r_f^2 + r_r^2 \left(1 - r_f^2\right)^2 + 2 r_f r_r \left(1 - r_f^2\right)^2 \cos\left(2kdn_p \cos q' + f_f - f_r\right) \right] \quad (6)$$

As in Eq. 5, r_f, ϕ_f and r_r, ϕ_r are respectively the magnitude and the phase of the Fresnel reflection coefficient for the front and rear interfaces of the particle. The terms d and n_p denote its diameter and refractive index respectively. The black spectra are obtained using Mie theory from Eq. 7 [26].

$$\left|s_b(k)\right|^2 = \frac{1}{2} \sum_{\theta \in NA} \left[\left| \sum_{\alpha \in \Omega} E_s^{\parallel}(k,\theta,\alpha) \right|^2 + \left| \sum_{\alpha \in \Omega} E_s^{\perp}(k,\theta,\alpha) \right|^2 \right]$$
$$\begin{pmatrix} E_s^{\parallel}(k,\alpha) \\ E_s^{\perp}(k,\alpha) \end{pmatrix} = \frac{e^{-ikr+ikz}}{ikr} \begin{pmatrix} S_2(k,\alpha) & 0 \\ 0 & S_1(k,\alpha) \end{pmatrix} \begin{pmatrix} E_i^{\parallel} \\ E_i^{\perp} \end{pmatrix} \quad (7)$$

with $E_i^{\parallel,\perp}$ as the amplitude of the incident electric field for the polarizations s and p and $S_{2,1}$ as the scattering amplitude for the same polarizations [26]. The exponential term refers to the fact that the scattered wave is spherical. The coefficients $S_{2,1}$ of the scattering matrix are calculated from the associated Legendre polynomials and the Ricatti-Bessel functions [27, 28]. If we denote by θ the incidence angle, the backscattering spectrum is obtained by summing the scattered intensity of both polarizations over the numerical aperture (NA). For each polarization and incidence angle, the scattered intensity is equal to the sum of the scattered electric field in the region Ω. This region defines the scattering angles α for which the scattered wave is collected by the objective. Fig. 4 shows that for an incidence angle θ, the region Ω is defined as the oriented angles α for which: $\pi - \theta + \theta_{max} \geq \alpha \geq \pi - \theta - \theta_{max}$.

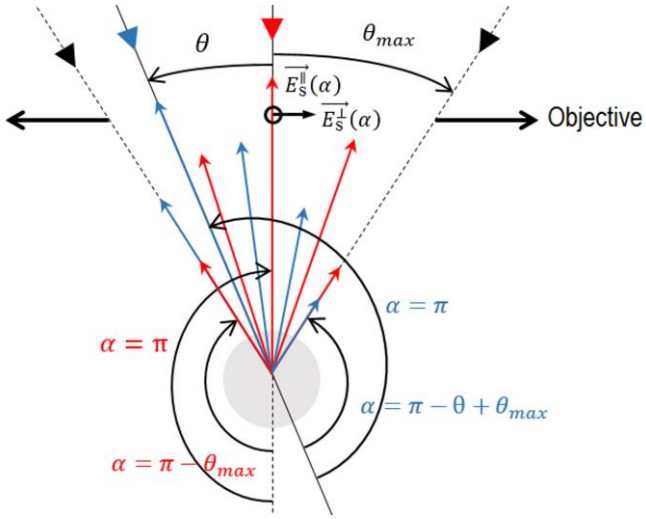

Fig. 4. Schematic representation of the light/particle interaction for computing the backscattering spectrum.

Because we will see that the coherence length is about 2 µm in our optical arrangement, only the particles that meet the condition OT << 1 µm can be described using the backscattering spectrum given in Eq. 7. Although this model is not used in this paper because the work focuses on the characterization of micrometric particles featuring an OT that always far exceeds 1 µm, we wondered whether the proposed technique could work in the case where Mie theory was used. To check this possibility, the interference signal of the particle has been calculated for this particular case. All the light backscattered in the region Ω participates in the interference phenomenon and has to be taken into account. As an example, the red and blue rays in Fig. 4 represent the amount of light that is collected by the objective after the scattering of the plane wave with a normal incidence and an incidence of θ respectively. Assuming the scattered spherical wave to be a plane wave after passing through the objective and because of the far-field observation of the interference, the expression of the backscattered electric field is as simple as $S_{1,2}(\alpha,k)s(k)$ (1 and 2 refer to the polarization) with $s(k)$ the incident electric field amplitude. Its development leads to Eq. 8.

$$I_{\parallel,\perp}(z) = 4\pi \sum_{k} \sum_{\theta \in NA} S(k)\,\mathrm{Re}\left[\sum_{\alpha \in \Omega} S_{2,1}(k,\alpha)\, r_{ref}^{\parallel,\perp *}(k) \exp(j2kz\cos\theta)\cos(\theta)\sin(\theta)\, d\theta\, dk \right] \quad \textbf{(8)}$$

The coefficient $r_{ref}^{\parallel,\perp *}$ denotes the conjugate of the amplitude reflection coefficient of the reference mirror for the s and p polarizations and the exponential term represents the phase shift between the reference mirror and the top surface of the bead. Because a non-polarized light source is used, the final interferometric signal acquired by the camera is the sum of $I_{\parallel}$ and $I_{\perp}$. By applying this formula to the previous study of a polystyrene bead (n = 1.58, r = 1.5 µm) buried in a transparent medium (n = 1.4), it can be observed that the fringe contrast is strongly attenuated and that the second interferogram, related to the back surface reflection, vanishes (Fig. 5).

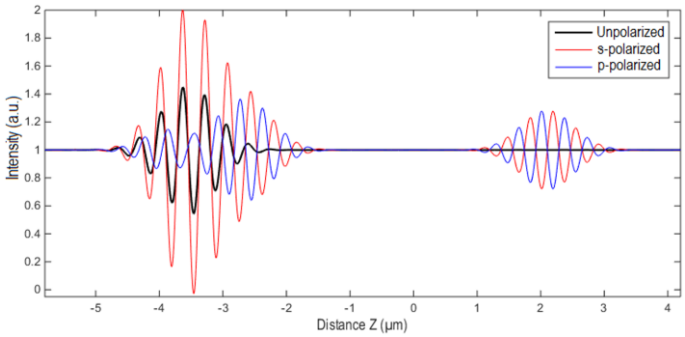

Fig. 5. Theoretical interferometric signals of a polystyrene bead with a 3 µm diameter included in a transparent medium with a 1.4 refractive index. The black, red and blue signals are respectively obtained with an unpolarized, s-polarized and p-polarized illumination source.

This is explained by the fact that the scattered waves for the s and p polarizations are exactly in antiphase (π phase difference) in the case of backscattering [29]. Because of the almost complete suppression of the signal, the actual backscattering spectrum of the bead cannot be retrieved from the spectral analysis of the interference

signal, preventing any further characterization. However, it is worth noting that according to our simulations, the method is usable if the light source is only s or p-polarized.

3. Experimental details

A. Optical set-up

1. System description

The optical system used to carry out the experiments is presented in Fig. 6. This consists of a modified Leitz-Linnik interference microscope with two identical 50x objectives (NA = 0.85) and an incandescent lamp illumination source. By taking into account the spectral response of the camera, the illumination source spectrum is almost Gaussian with a spectral bandwidth and a central wavelength of respectively 280 nm and 800 nm. The first three lenses, named L_1, are located so as to obtain a Köhler illuminator allowing homogeneous illumination of the sample after passing through the objectives. The aperture diaphragm (AD) enables the control of the illumination angle as well as the spatial coherence of the source. After being reflected on both the reference mirror and the sample, the light interferes and is focused onto the camera by the imaging lens L_2. In this configuration, the image acquired by the camera consists in the image of the sample with white fringes superimposed on its surface.

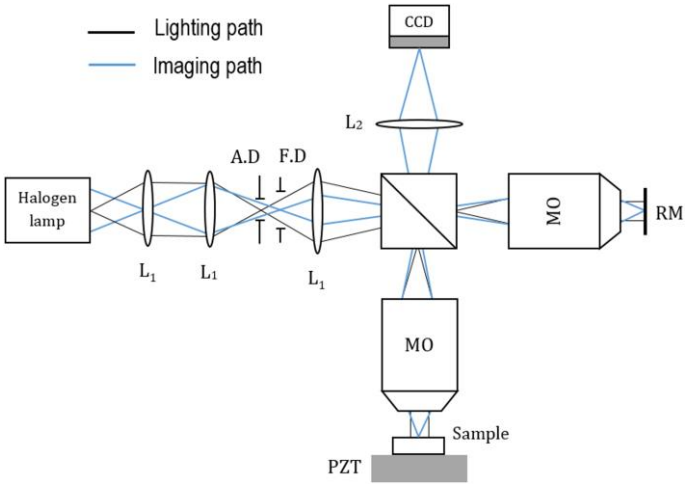

Fig. 6. Schematic diagram of the optical system. L1, aspheric lenses; L2, imaging lens f = 200 mm; A.D, aperture diaphragm; F.D, field diaphragm; MO, 50x microscope objectives; RM, reference mirror; PZT, piezoelectric table.

The sample is then investigated over depth by changing the distance between the reference mirror and the sample surface. This is attained by using a piezoelectric table (PIFOC from PI) located under the sample. The piezo actuator is controlled in a closed loop with a capacitive position sensor, having a sensitivity of 1 nm. At each displacement step, the fringes are scanned over the vertical axis and an image is acquired with the camera, leading to the interferometric image stack as illustrated in Fig. 2. The signal acquisition is performed with a

Photonfocus monochrome camera having 1024x1024 pixels and a Giga Ethernet connection. With respect to the Nyquist-Shannon sampling theorem, the displacement step is adjusted to 50 nm, which ensures a sufficient sampling of the interferometric signal with a frequency several times above the Nyquist frequency. The whole system is controlled using a program developed in LabVIEW 2016 with the Imaq Vision module.

One of the main interests of interferometric data for such characterization obviously relies on the possibility of carrying it out with a very high spatial resolution. Using interference microscopy, the measurements are 3D-resolved so as both the transverse and axial resolutions need to be clarified. The values of the lateral and axial resolutions are crucial because they refer to the smallest sized particle that can be characterized independently from the rest of the sample.

2. Lateral resolution

Because the method only consists in the analysis of the signal spectral content, the lateral resolution of the measurement will be given either by the area required to extract this signal or by the resolution of the optical system. Usually, we use an area of 3x3 pixel binning corresponding to a surface of 0.34 µm x 0.34 µm (0.12 µm²), in order to reduce temporal noise from the camera. As regards the resolution of the optical system, this is given as in any imaging device, by the Full Width at Half Maximum (FWHM) of the Point Spread Function (PSF), which is, in the case of a diffraction-limited optical system, the Airy function (Eq. 9) [21].

$$h(u) = \left[\frac{2J_1(u)}{u}\right]^2, u = \frac{2p}{l} r \cdot NA \qquad \textbf{(9)}$$

where J_1 depicts the Bessel function of the first kind and first order. Assuming the Rayleigh criterion in the case of incoherent illumination, the lateral resolution is approximately defined by the radius of this function, which is $\Delta x = 0.61\lambda_0/NA = 0.57\ \mu m$ with λ_0 as the central wavelength of the source spectrum. This leads to a surface of $\pi\Delta x^2$ being well above the area delimited by 3x3 pixels. Consequently, the lateral resolution will be then limited by the resolution of the optical system.

Moreover, we already demonstrated for the inspection of transparent layers the need to reduce the effective NA to obtain spectra free from errors [25]. This effective NA reduction is attained by closing the aperture diaphragm and necessarily involves an increase in the degree of spatial coherence of the system. Indeed, we recall that the spatial coherence of the system (~ effective NA) is controlled by both the NA of the illumination (defined by the AD) and the NA of the objective [30]. This leads to a decrease in the lateral resolution.

Experimentally, many criteria and methods have been introduced to estimate the resolution of an optical system, such as the measurement of the 10-90% rise distance of the intensity profile along a perfect edge [31,32], from the imaging of two pinholes of equal brightness [30] or from the measurement of the Modulation Transfer Function (MTF). In our case, it is the latter that was used to determine the resolution loss induced by the closing of the AD. The results shown in Fig. 7 demonstrate cut-off frequencies of 2 lines/µm and 1.2 lines/µm for the AD in the open and closed positions respectively. This results in a lateral resolution of about 0.83 µm (with a

loss of 0.33 µm). In accordance with the theory, we also note that increasing the degree of spatial coherence of the illumination involves a better contrast for the smaller spatial frequencies.

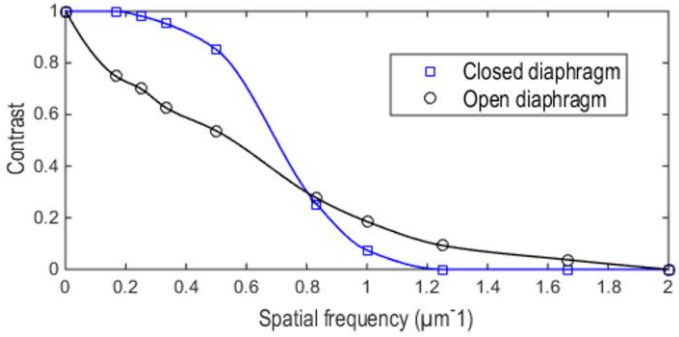

Fig. 7. Modulation transfer function of the optical system for two extreme positions of the aperture diaphragm.

3. Axial resolution

In interference microscopy, the axial resolution is commonly defined as the FWHM of the fringe visibility [33]. In the general case, this envelope is adjusted by both the temporal and spatial coherence of the system [34]. The former is proportional to the coherence length of the source while the latter only depends on the numerical apertures of the objective and the illumination. As a result, the axial resolution is mainly governed by either the properties of the source or by the effective NA of the system. Although it only affects the spatial coherence, the fact of closing the AD during the acquisition will obviously degrade the resolution. To theoretically check how the axial resolution would be modified, the influence of each term (temporal and spatial coherence) has been studied and the resulting resolution plotted as a function of the effective NA [25]. Because of the very low coherence length of the source, it appears that the effect of the temporal coherence is so predominant compared to the spatial effect that decreasing the illumination NA is nearly insignificant. It follows that the axial resolution remains almost identical whatever the extent of the AD being closed. By measuring the FWHM of two interferograms for the AD fully open and closed as much as possible we found the axial resolution to be 1.05 µm and 1.08 µm (Fig. 8).

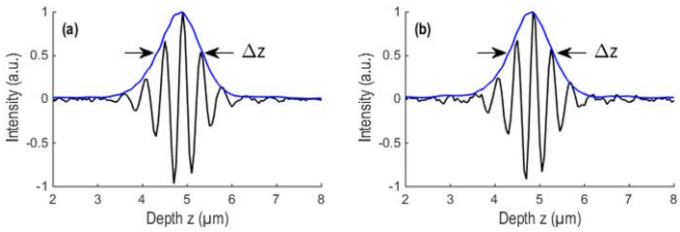

Fig. 8. Experimental axial resolution for two extreme positions of the AD. (a) Fully open. (b) Closed as much as possible. The interferograms are recorded from a silicon substrate.

The resolution value Δz illustrated in Fig. 8 and equal to 1.08 µm corresponds to the imaging resolution but not to that achievable for the spectral characterization. Indeed, as shown in Fig. 9, the actual resolution of the measurement is slightly larger than Δz and depends not only on the system properties but also on the sample

features such as its dispersion. The axial resolution is defined as the minimal distance between the adjacent surfaces of two particles that can be measured independently and was found to be approximately $2.3 \times \Delta z = 2.85\ \mu m$. This is explained by the fact that two successive structures along the depth can be studied independently of each other only if their signals are sufficiently spaced to be processed separately. Indeed, we recall that the characterization method relies on the spectral analysis of the only interference signal of the particle studied. In the rigorous case of imaging, the interferograms over Z can be mixed as long as their envelope peaks are easily identifiable, allowing a clear discrimination of both structures. As an example in Fig. 9, it will be possible to characterize particle "1" as long as it is separated from particle "3" by Δx and that the top surface of "1" is separated from the bottom surface of "2" by 2.3Δz.

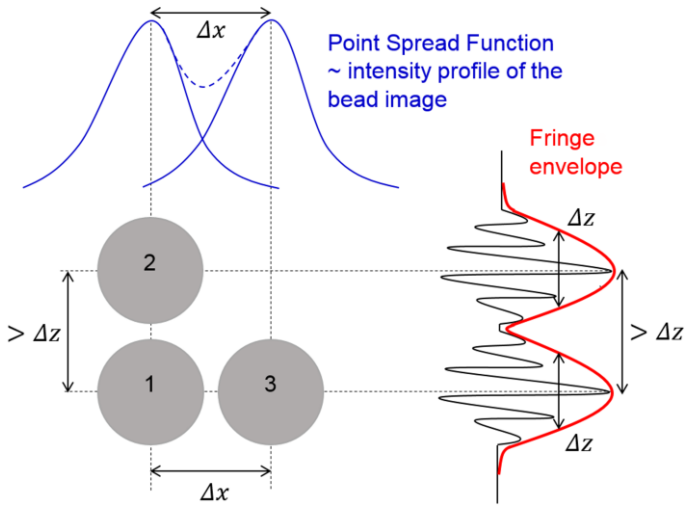

Fig. 9. Spatial resolutions of the characterization method. The lateral resolution is equal to that classically defined in microscopy imaging Δx. The axial resolution is larger than that used in interference microscopy imaging and approximately equals $2.3\Delta z$. In this scheme we supposed that the signals from the top and bottom surfaces of each particle were mixed together leading to one global interferogram. Rigorously, the resolution $2.3\Delta z$ indicates the separation between the top surface of "1" and the bottom surface of "2".

B. Signal processing (total reflectance spectrum)

As explained in sections 2.A and 2.B, the backscattering spectrum from which will be extracted the properties of the structure studied is obtained from Eq. 4 and requires two distinct steps. The first one is called the calibration step and consists in measuring a sample with a known spectral reflectance in order to determine the spectral signature of the system (STF) for the given experimental/surrounding conditions. In our case, a silicon substrate is used and was measured using a UV-VIS-IR optical spectrometer at λ_m points. These points are spaced by 1 nm and linearly distributed in the range [450 nm; 1100 nm]. The second step, called the measurement step, is quite similar and is applied to the sample to be characterized.

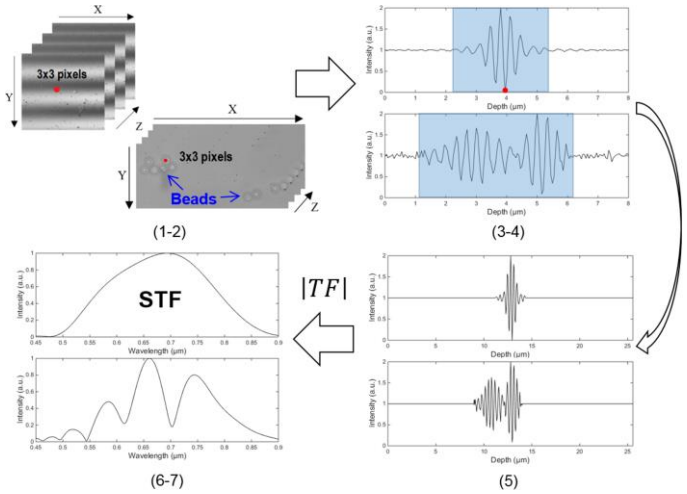

Fig. 10. Processing procedure. Each step is indicated by his associated number. The upper image stack is the one of the calibration sample (silicon substrate) whose the processing leads to the STF. The lower stack represents silica beads deposited on a glass substrate. The backscattering spectrum is then obtained by squared division of the oscillating spectrum by the STF.

The whole procedure involved in these two previous steps is detailed below:

1. Loading of the image stack into the RAM.
2. **Selection of the area to be characterized (signal extraction).**
3. Use of an envelope extraction algorithm (low pass filter) followed by a peak detection algorithm to locate the positions of the different interferograms.
4. **Selection of the part of the signal to be analyzed (spatial length) using an apodisation window.**
5. Increase of the number of points in the part of the signal selected by means of a zero-padding algorithm.
6. Fast Fourier Transform (FFT) of the signal. For the Fourier analysis, we use $\delta = 2z$ and $\sigma = 1/\lambda$ as direct and conjugate variables respectively.
7. Linear interpolation of the spectrum at λ_m points.

The points in bold are specifically intended for the measurement step. Indeed, the calibration signal is always extracted from the same area to overcome the responses that may be slightly different from one pixel to another. In addition, the length of the calibration signal automatically adjusts to that of the measurement signal and the window is automatically centered on the maximum amplitude of the interferogram. The entire procedure is graphically represented in Fig. 10. As mentioned in Section 3.A.3, the interferograms are usually spread over a small distance of the order of 2.85 µm due to the use of a broad white light spectrum. This will then correspond to the minimal size of the apodisation window. In order to select the more appropriate length of the signal, several factors need to be considered. Indeed, while larger windows would be more suitable for obtaining a high spectral resolution, this would lead to the inclusion of too much noise in the calculation from the parts of the signal outside the 2.85 µm wide interferogram, where the signal to noise ratio (SNR) is very low. As is shown in Fig. 11, taking a wider window leads to unwanted oscillations in the spectrum (S_2) and generates discrepancies

compared to the theoretical spectrum (S_S). By using a narrower window, S_1 is obtained by using a 3 µm wide signal, the oscillations vanish, and the spectrum becomes closer to S_S. We will also see that this noise (~ SNR level) has a significant influence on the accuracy of the characterization. As a result, the window size is generally the same as that of the signal of interest (which, for large particles, necessarily includes the interferograms from both the top and back interfaces).

Because it is primordial to keep the noise as low as possible, the only way to increase the spectral resolution would result from having an interferogram larger over Z, which would decrease the axial resolution. In our case, the ability to measure the properties of a single particle regardless of the other sample constituents relies on the ability to correctly separate the interferograms along the Z-axis. We have therefore chosen to favor a good axial resolution over the spectral resolution.

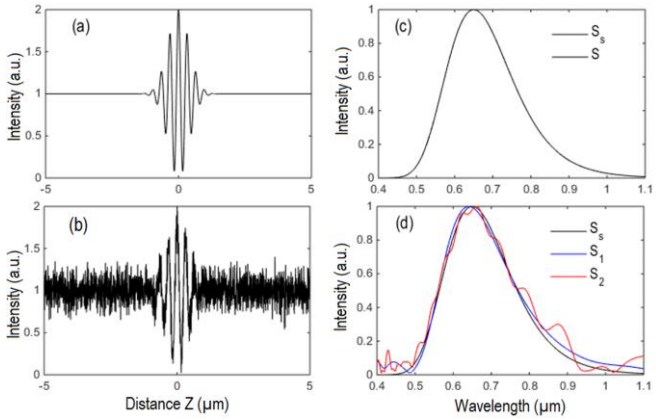

Fig. 11. (a-b) Simulated interference signals with (a) no noise (b) additive white Gaussian noise leading to a signal to noise ratio of 10.45 dB. (c-d) Comparison between the expected theoretical spectrum (S_S) and the spectra calculated from the FT of the signals in (a-b). In the case (c), the spectrum S is very close to S_S whatever the length of the window. In the case (d), S_1 and S_2 are respectively obtained by using a 3 µm and 10 µm wide window.

The achievable spectral resolution then depends on the size of the particle studied and is defined as the FWHM of the Fourier transform of the window. For instance, by using a Hamming window in the case of a 2 µm particle with a constant refractive index of 1.6, the length would be 6 µm, leading to a spectral resolution equal to 378 cm^{-1} (24 nm at a wavelength of 800 nm). Before being Fourier transformed, each signal is increased in size to 4096 points using a zero-padding loop. This operation enables the sampling of the spectrum to be increased: $\delta\sigma = (2\delta z N)^{-1} = 24 cm^{-1}$ (1.5 nm at a wavelength of 800 nm) with δz as the piezo displacement step (50 nm) and N as the total number of points (4096).

C. Adjustment non-linear algorithm

As mentioned in Section 2, the method combines experimental measurements with theoretical models to recover the properties of the particle. Once the experimental backscattering spectrum is obtained and the model describing correctly the interferometric spectral response of the particle is chosen, the next step is to match them together. The idea is therefore to bring the model to converge towards the experimental data by optimizing the value of the parameters that are sought. In our case, these parameters are the refractive index and the size of the particle. Since the phase and the magnitude of the backscattering spectrum contain the information on both the size and the refractive index of the particle, one or the other could be used as a model as in the case for thin film analysis [35-37]. Because we evaluated the magnitude as being the best way for having the most sensitive measurement [38], only the spectrum magnitude was used. Both the experimental and theoretical spectra were sampled at the same N points where k_1 and k_N span the spectral range used to match the model to the data. To assess whether the fit between the experimental and theoretical data is optimized, an error function χ defined as their quadratic error is used.

$$\min_{d,n_p} c(k) = \min_{d,n_p} \sum_{i=1}^{N} \left[\left| s_p(k_i, d, n_p) \right|^2 - y_{data}(k_i) \right]^2 \qquad \textbf{(10)}$$

The parameters d and n_p denote respectively the diameter and refractive index of the particle, s_b is the model of backscattering spectrum as defined in Eq. 6 and y_{data} is the experimental spectrum. Because of the non-linearity of the spectrum magnitude, a multidimensional nonlinear algorithm is used to converge towards the best solution. The Levenberg-Marquardt algorithm, based on the least-squares method and available in the MATLAB software has been used since it appeared to be the most commonly used algorithm for such characterization. Usually, this kind of algorithm cannot immediately provide the global minimum of χ (~ the best solution) since there may exist multiple local minima [35, 39, 40]. The algorithm provides only one of them depending on the initial value of the fitting parameters. Computationally speaking, we then used the same method as the one we detailed in [41] for the characterization of thick transparent layers. Basically, it consists in varying the initial values of the different parameters (d and n_p) within one given range and recording both the local minimum and the final error provided by the algorithm, which corresponds to the difference between the data and the optimized model. The global minimum is then obtained by identifying the iteration that leads to the lowest error and only requires a few seconds (~ 5s).

In the case of transparent layers, our method proved to be at the same time fast, robust and accurate [41]. However, in the case of micrometric particles, in particular for those contained in a complex medium, a much lower signal to noise ratio is expected, which may induce some errors in the optimization algorithm. With our experimental system, a SNR of ~ 36 dB was measured in the case of a simple transparent layer. The SNR is defined as the ratio between the maximal amplitude of the central white fringe (A_S) and the amplitude of the noise (A_N) as shown by Eq. 11. The noise amplitude is estimated by its standard deviation σ_N.

$$SNR_{dB} = 20\log\left(\frac{A_S}{A_N}\right) \quad with\ A_N = s_N \qquad \textbf{(11)}$$

For the study of micrometric particles contained in transparent media, the SNR can be significantly lower and may become less than 8 dB, especially in biological media where the refractive index contrast between each structures is in the order of 0.1 or even less. To assess its robustness to noise, the characterization technique has been tested on synthetic interference signals. The simulation consists in a 2 µm particle with a constant refractive index of 1.58 buried at a depth of 3 µm within a semi-infinite medium with an index of 1.48. The STF of the simulation is represented in Fig. 12 and shows that the wavelength domain used to determine the properties of the particle ranges from 0.5 µm to 1 µm.

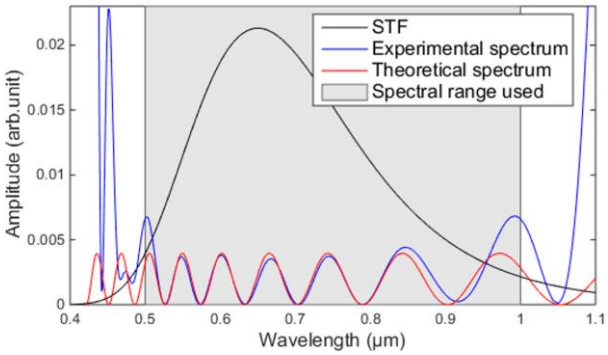

Fig. 12. STF used in the simulation. The grey area is the wavelength range having a sufficient SNR to allow an error-free fit between the experimental and theoretical backscattering spectrum of the particle. The experimental spectrum is obtained from the processing of noisy interference fringes while the theoretical spectrum corresponds to the model

Despite the fact that the use of a wider spectral range would facilitate the accurate determination of the particle properties, it is nevertheless essential to restrict this domain to one with a sufficient SNR in order to prevent any significant error during the matching process. As an example, we superimposed on Fig. 12 the theoretical backscattering spectrum of the particle (red curve) and the one obtained from processing a noisy interference signal of the particle (blue curve). It can be noticed that the areas of the blue spectrum that are outside the [0.5 µm; 1 µm] spectral range are very sensitive to noise and thus inevitably differ greatly from the theoretical spectrum (model). A white Gaussian noise is assumed for representing the different noise sources. Now limited to the [0.5 µm; 1 µm] wavelength range, four simulations were carried out, each of them with a different level of noise (SNR = ∞, 12 dB, 9 dB, 6 dB). The case where SNR = ∞ means the total absence of noise. The NA is set to 0.1 as we recall the necessity of using small apertures for spectral measurements [25]. The total interference signal and the windowed signal are represented in Fig. 13(a) for the case where SNR = 9 dB. The first interferogram is due to the light reflection on the sample surface. The backscattering spectra of the particle are plotted in Fig. 13(b).

The black curve corresponds to the spectrum obtained from the processing of the windowed fringes and the red curve is the optimized model, i.e., the model that uses the values of the diameter and refractive index given by the adjustment algorithm. These values are respectively 2.279 µm and 1.387 for the size and index of the particle and differ a lot compared to the theoretical values of 2 µm and 1.58. The Table 1 summarizes the values given by the adjustment algorithm for the cases where SNR = ∞, 12 dB and 6 dB.

Table. 1. Measurement of the bead size and refractive index for different SNR. The theoretical values are d = 2 µm and n = 1.58.

SNR (dB)	∞	12	9	6
d	2	2.296	2.279	2.346
n	1.58	1.38	1.387	1.344

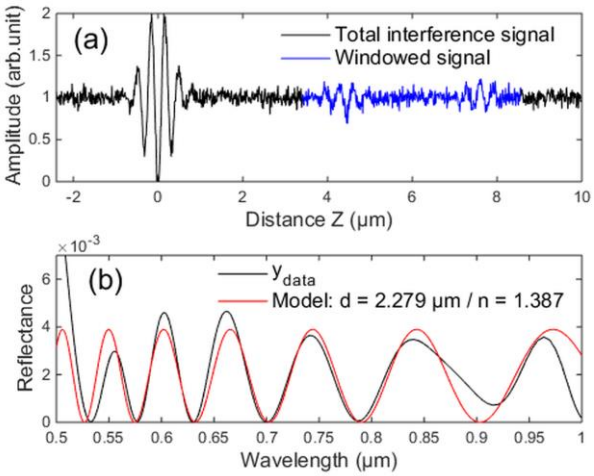

Fig. 13. (a) Simulated interference signal of a 2 µm particle contained in a transparent layer for a SNR of 9 dB. The blue signal is that of the particle. (b) Backscattering spectra. The black curve is obtained from the processing of the blue signal in (a) and the red curve is the model given in Eq. 6 that uses the values of e and n leading to the best fit.

As can be noticed from Table 1, the adjustment algorithm leads to wrong values as soon as the SNR is too weak, which will be frequently the case for the inspection of micrometric particles. In order to increase this SNR, a temporal averaging is performed during the acquisition of the data. In terms of simulation, this means that the final interference signal is produced from the averaging of N noisy signals. This simple processing enables a high attenuation of the noise and consequently improves the accuracy of the adjustment algorithm as shown in Fig. 14.

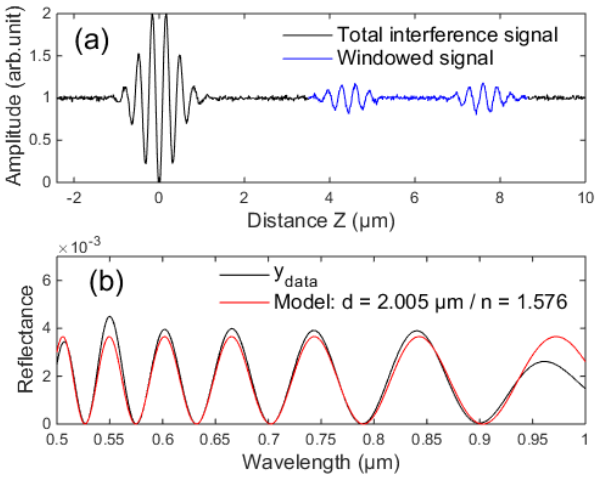

Fig. 14. (a) Simulated interference signal of a 2 µm particle contained in a transparent layer for an initial SNR of 9 dB. The signal results from the averaging of four noisy signal allowing the SNR to be improved. (b) Backscattering spectra. The black curve is obtained from the processing of the blue signal in (a) and the red curve is the model given in Eq. 6 that uses the values of e and n leading to the best fit.

The initial SNR is still set at 9 dB and the interference signal is computed from the averaging of four noisy signals. This time, it can be noticed that the values of both the thickness and the refractive index are completely consistent with the theoretical values. The same study was conducted for the cases where SNR = 12 dB and 6 dB with the results summarized in Table 2. Contrarily to what happened without averaging, the values are all very close to the theoretical values even in the worst case (SNR = 6 dB). Although these are only simulations and they certainly do not take into account all the possible sources of signal degradation that may occur during a real measurement, it is sufficient to demonstrate that performing processing as simple as a temporal averaging enables the accuracy of the method to be improved.

Table. 2. Measurement of the bead size and refractive index for different SNR and after applying an averaging of 4 signals. The theoretical values are d = 2 µm and n = 1.58.

SNR (dB)	∞	12	9	6
d	2	2.002	2.005	2.009
n	1.58	1.58	1.576	1.573

4. Results: Silica and polystyrene beads

In this section, the method is applied to silica (from Cospheric) and polystyrene (from EPRUI Biotech) beads with the purpose of simultaneously retrieving their size and refractive index. For all the results presented in sections A and B, the interferometric signals from which the backscattering spectra are computed are obtained by using temporal averaging during the acquisition of the data. This means that N consecutive images are averaged together at each piezoelectric displacement step and only the resulting image is recorded [42]. In order

not to increase the acquisition time too much, N was chosen to be equal to 4, which still allows a noise reduction of a factor 2.

A. Verification of the beads diameter and uncertainty

In order to accurately estimate the size of the beads and the associated uncertainty, the first experiments were carried out on beads located at the surface of a glass substrate. Indeed, these being located at the surface, an estimation of their size without taking into account their refractive index was possible by looking at the relative position of the signal envelope peak from the top of the bead and that of the substrate as shown in Fig. 15. Moreover, this configuration makes it possible to work with a high SNR. Indeed, this maintains a good fringe contrast as the refractive index variation between the air and the particle is high and the SNR level is directly related to the contrast of the fringes. The beads, being supplied either in powder form or within a solution, were mixed in water and then deposited by spin coating. The purpose was to avoid the creation of aggregates to obtain a fairly homogeneous distribution on the substrate. Since the refractive indices of both the bead and the glass substrate are only real and higher than 1, the same phase shift of π occurs during the light reflections on the interfaces air/bead and air/substrate. Consequently, the slight shift of the interferogram peak induced by phase change on reflection [33] is the same for both signals and do not lead to errors in the calculation of the diameter. Fig. 15 shows several measurements of the diameter of the silica beads, which are equal in theory to 4.08 and 1.70 µm for cases (a) and (b) respectively.

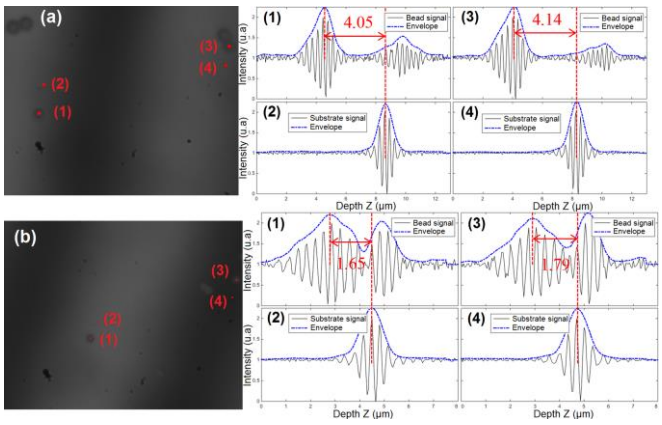

Fig. 15. Extraction areas of interferometric signals to determine the diameter of the beads. (a) 4.08 µm. (b) 1.70 µm. The zones (1) and (3) are chosen for being at the top of a bead. The zones (2) and (4) are chosen for being on the substrate and are exactly on the same fringe in order to avoid any errors due to the sample tilt. The signals from areas (1)-(2) and (3)-(4) are respectively put alongside so that they are used to obtain the bead diameter.

Even though the diameters measured are in accordance with the data specified by the supplier, we noticed by repeating the measurements on a large number of beads over the field of view that the diameter can vary by several hundred nanometers. We estimated the uncertainty to be about 3.5 % whatever the size, leading to a precision of 4.08 ± 0.14 µm and 1.70 ± 0.06 µm. The same work was performed on polystyrene beads having a theoretical size of 3 and 2 µm. In this case, the uncertainty was estimated to be slightly lower and equal to 3 %.

B. Particles located within a transparent layer of Gelatin

The silica and polystyrene beads have been studied in such a way as to reach similar approaches used for the study cases of biological samples or transparent materials. This means that the particles have to be buried within the depth of a transparent or scattering medium. The latter case is studied theoretically in section C.

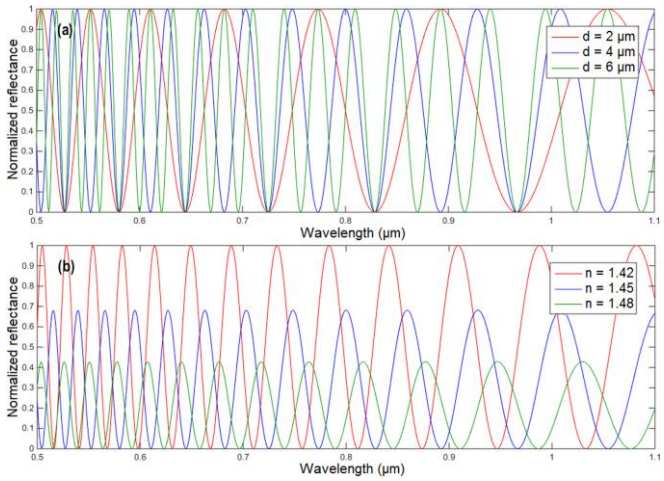

Fig. 16. Theoretical backscattering spectrum of a bead contained in a medium with a constant refractive index of 1.6. (a) The refractive index of the bead is 1.45. (b) The diameter of the bead is 4 µm

The theoretical backscattering spectrum of a bead located in a transparent medium with a constant refractive index of 1.6 is plotted in Fig. 16. We first consider the case of a bead with a constant refractive index and three different sizes (a) and then the case with a constant size and different indices (b). It is worth noting that while the diameter d only changes the oscillation frequency of the spectrum, the refractive index n_p is related to both the frequency and the amplitude of these oscillations. It is therefore essential for the spectrum amplitude not to be biased (which is for instance the case when using a large NA) so that the determination of the index is error-free. In addition, an error in the measurement of the index would necessarily imply an error in the measurement of the size. By taking a closer look at the influence of the noise on the backscattering spectrum of a polystyrene bead (Fig. 17), it can be observed that the noise introduces more errors in the amplitude of the oscillations than in the location of the peaks. Consequently, it can be assumed that the precision of the refractive index measurement will be much more sensitive to the SNR than the measurement of the size.

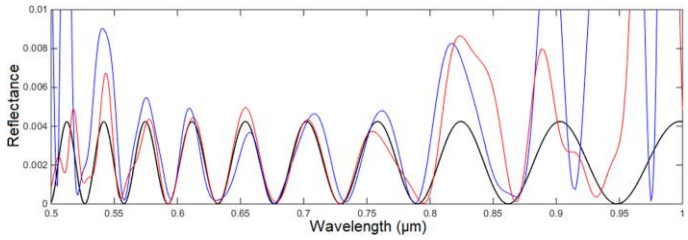

Fig. 17. Simulated backscattering spectra of the polystyrene bead for different SNR. The black, red and blue curves are respectively obtained with a SNR of +∞, 8.8 dB and 6 dB.

The sample was manufactured in our lab by depositing the beads in a layer of gelatin (photographic gelatin for holography). The gelatin was mixed in water (5 % of the total volume) at 50°C with magnetic stirring. Once the mixture was homogeneous, the beads were added to the solution with magnetic stirring in order to obtain a homogeneous distribution of the beads. The solution was poured onto preheated microscope glass slides, which were then cooled down to solidify the deposit. Measurement with a mechanical profilometer indicated a thickness of about 40 µm. The gelatin index was measured to be on average 1.48 using a refractometer. The sample contains a mixture of all the beads (both materials and all sizes). Such a test sample makes it possible to test the capacity of the method for spectrally discretizing and identifying particles of different natures and sizes.

The model used to recover the properties of the beads assumes a wavelength-independent refractive index. For these studies, this hypothesis is sufficient since silica and polystyrene are both very small dispersive materials, with an average refractive index of 1.45 and 1.58. Nevertheless, we demonstrated the possibility to recover the wavelength dependency of the refractive index. The only need is to express the optical index from a dispersion law (Cauchy or Sellmeier) and to use the parameters of these laws as optimization variables in the adjustment algorithm [41]. The beads being distributed very homogeneously, several acquisitions of the sample were required as we tried to measure each different kind of bead at least 3 times. It appeared that all the 4.08 µm silica beads were found to be located right below the surface, thus preventing their characterization since the fringes from the top of the bead were mixed with those from the surface. As a result, it was only possible to measure the 1.70 µm silica beads and 2-3 µm polystyrene beads. Once a bead was found in the layer, its size and refractive index were measured by using the algorithm given in Eq. 10 (Model 1). After identifying whether the bead was silica or polystyrene, the characterization was performed again by using the same model except that a theoretical refractive index of the bead was used in the algorithm and therefore only the size was sought (Model 2). The purpose of the previous approach was to estimate whether the measurement of the diameter is much more accurate when not taking into account the index measurement that is probably more sensitive to noise. When using Model 2, the refractive indices of the polystyrene and silica are respectively obtained from [40] and [41]:

$$n_{PS}^2 = 1 + \frac{1.4435/^2}{/^2 - 0.020216}$$
$$n_{SiO_2}^2 = 1 + \frac{0.696166/^2}{/^2 - \left(0.0684043\right)^2} + \frac{0.4079426/^2}{/^2 - \left(0.1162414\right)^2} \quad \textbf{(12)}$$

Two examples of characterization for respectively a bead of polystyrene (2 µm) and silica (1.70 µm) are given in Figs. 18 and 19.

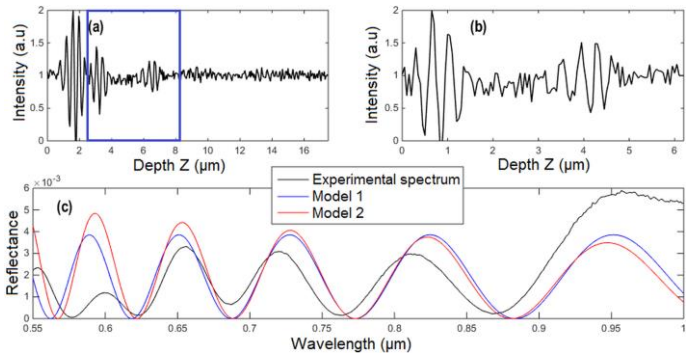

Fig. 18. (a) Total interference signal of the sample. (b) Windowed signal from the blue square in (a) including the fringes from the top and bottom sides of a 2 µm polystyrene bead. (c) Comparison between the experimental backscattering spectrum (black curve) and the optimized models set by the size and the index (Model 1) or just the size (Model 2). We found respectively d = 1.959 µm and n = 1.579 for M_1 and d = 1.957 µm for M_2.

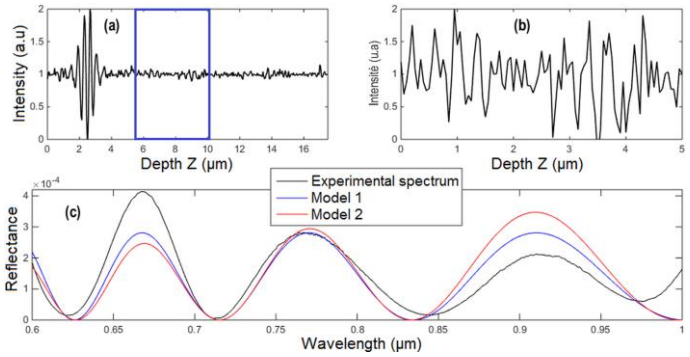

Fig. 19. (a) Total interference signal of the sample. (b) Windowed signal from the blue square in (a) including the fringes from the top and bottom sides of a 1.70 µm silica bead. (c) Comparison between the experimental backscattering spectrum (black curve) and the optimized models set by the size and the index (Model 1) or just the size (Model 2). We found respectively d = 1.721 µm and n = 1.454 for M_1 and d = 1.720 µm for M_2.

For each case, the total interference signal of the sample, which is extracted from the acquired image stack, is plotted in (a) and the windowed portion from which is computed the backscattering spectrum is displayed in (b). The resulting backscattering spectrum is plotted in black in (c). The blue and red curves are the optimized models of the backscattering spectrum when using both the diameter and the index (blue) or only the diameter (red) as fitting parameters. In the case of the polystyrene bead, the refractive index variation between the bead and the layer is small, i.e. ~ 0.1, and we thus estimated the SNR to be ~ 9 dB after averaging. Using Model 1, values of 1.959 µm and 1.579 are respectively obtained for the diameter and refractive index. Using Model 2, a diameter of 1.957 µm is calculated. All these values match the expected ones (2 µm and1.58).

In the case of the silica bead, the variation of the refractive index is even lower, i.e. about 0.03, leading to a SNR of less than 6 dB despite the averaging. In this case, we obtain d = 1.721 µm and n = 1.454 with Model 1 and d = 1.720 µm using Model 2. These values are all in agreement with the theoretical data (d = 1.70 µm and n = 1.45). These characterizations were repeated several times as each type of bead was measured between 3 and 5

times. The summary of the results obtained, including the mean value, the standard deviation and the relative error (compared to the provider data) for each bead and each model are given in Table 3. The relative error (R.E) is calculated as the average of the relative errors of each value measured and not from the error of the mean value (M.V). It can be noticed for each type of bead, whether for the size or the index, that the standard deviation is relatively low, thus proving the repeatability of the measurements. As regards the results on the mean values and the relative errors, several comments need to be made. First, in a general way, the measurement of both the size and the refractive index are far from being imprecise and are globally satisfactory enough for clearly identifying the bead. Nevertheless, the measurement of the size seems better than that of the refractive index since the latter is obtained with an error to a value of 0.1, which can be quite high when searching with precision the refractive index of a particle. Moreover, we notice that the measurement of the size is by far more accurate when using Model 2 that takes a theoretical value for the index. This is explained by the reduced sensitivity of the model to the noise-induced amplitude disparities. In addition, the relative errors become included in the uncertainty area previously estimated. All these experimental observations go in the same direction as the simulations. They also validate our hypothesis stating that the determination of the refractive index is more sensitive to noise and further introduces more errors in the calculation of the diameter. They emphasize the obvious need to obtain high quality and low noise interference signals for such accurate morphological characterization.

Table. 3. Summary of the size and refractive index measurements of polystyrene and silica beads. M.V, Mean Value; S.D, Standard Deviation; R.E, Relative Error.

Kind of bead			Model 1						Model 2		
Material	d (µm)	n	d (µm)			n			d (µm)		
			M.V	S.D	R.E (%)	M.V	S.D	R.E (%)	M.V	S.D	R.E (%)
Polystyrene	3	1.58	3.255	0.054	8.50	1.610	0.010	1.80	2.982	0.125	4.17
Polystyrene	2	1.58	2.086	0.104	5.33	1.552	0.017	1.79	1.987	0.032	1.56
Silica	1.70	1.45	1.744	0.023	2.60	1.441	0.013	0.91	1.729	0.008	1.70

C. Simulation: particles located within a scattering medium

In the previous section, we presented the characterization results of spherical beads contained in a transparent layer.

The application of interference microscopy is obviously not limited to such simple samples and is precisely well known for studying more complex media, mainly through the inspection of biological tissues by OCT systems. In this section, the possibility of using the proposed interferometric method in the presence of a scattering medium is studied theoretically by means of simulation programs. Scattering is the main phenomenon occurring in biological matter and often leads to more complex measurements. In order to test the method, the first step was to develop an approach for simulating an interference signal in such complex media.

1. Modeling of the interference signal in a scattering medium

In most scattering media, light may undergo several scattering phenomena during its propagation before interacting with the studied structure. In this case, a random phase term is added in the phase shift between the reference wave and the object wave. This random phase is directly related to the optical path taken by the ray and therefore depends on the properties of the scattering medium. In our approach, we assume a static sample (stationary scatterers) and therefore a time-independent phase. When using interferometric methods, the reference wave allows the ballistic part of the light reflected by the structure to be selected. As a result, the portion of scattered light, whose phase randomly varies, is ignored since it interferes for different optical paths. This random variation of phase will certainly modify the interferometric signal and the associated spectrum because only the portion of ballistic light will participate in the formation of the fringes. In order to estimate the proportion of coherent light participating in the formation of the interference signal, it is essential to know the properties of the scattering medium. In our model, this will be characterized by:

- its scattering coefficient μ_{diff}. This describes the attenuation of collimated light passing through the medium. The mean free path (l_{diff}), i.e. the distance traveled by a photon between two successive scattering events, is equal to its inverse.
- the phase function p which gives information about the radiation pattern. This gives the probability for a photon to be scattered in a specific direction.
- the factor of anisotropy g which characterizes the anisotropy of the scattering.

To specify how the scatterers affect the light, it is necessary to associate a phase function to the medium. Depending on the size of the scatterers, the Rayleigh or Mie phase function are often used and enable very precise calculations on the angular distribution of the light scattered. In our simulation case, very precise information about the angular dependence of the diffusion is not required because the only interest is to obtain the probability for the light to be deviated in a given direction according to the medium properties. For practical reasons and mathematical simplicity, other phase functions were introduced [45-48]. Our choice was finally to work with the Henyey-Greenstein phase function given in Eq.13. This function depends on a single parameter g corresponding to the anisotropy factor. It has the advantage of representing at the same time the cases of backscattering (g = -1), forward scattering (g = 1) and isotropic scattering (g = 0) which is very useful when simulating a medium that contains a distribution of scatterers with different sizes. Depending on the scattering regime, the scattering efficiency is either proportional to the inverse of the wavelength raised to the power of 4 (Rayleigh) or non-wavelength-dependent (Mie). It is assumed in our case that all the wavelengths are scattered in the same proportion, corresponding to the study of a medium with scatterers that are large compared to the wavelength.

$$p_{HG}(q) = \frac{1}{4p}\frac{1 - g^2}{\left(1 + g^2 - 2g\cos q\right)^{3/2}} \qquad \textbf{(13)}$$

with -1 < g < 1 the anisotropy factor.

The purpose is to determine the proportion of coherent light participating in the formation of the interference signal. The light rays that are deviated by the scatterers have random phases that tend to add noise and decrease the quality of the interferometric signal. The assumptions made for calculating the random phase are as follows:

- the particles are spherical so that the scattering direction is independent from the azimuthal angle.
- the cross sections of the scatterers (ratio between the scattered energy and the incident intensity) are independent from the wavelength.

The scattering sample is illuminated by polychromatic light whose incident directions correspond to the angles defined by the numerical aperture of the objective. The calculation method is based on the decomposition of each incident plane wave and each wavelength into a sum of N rays having independent random phases. The same ray can be scattered several times. The propagation pattern of a ray within the medium is given in Fig. 20. This illustrates the path of three different rays undergoing either none, one or more scattering phenomena. The photons following these paths are considered to be ballistic, slightly diffused and strongly diffused photons respectively.

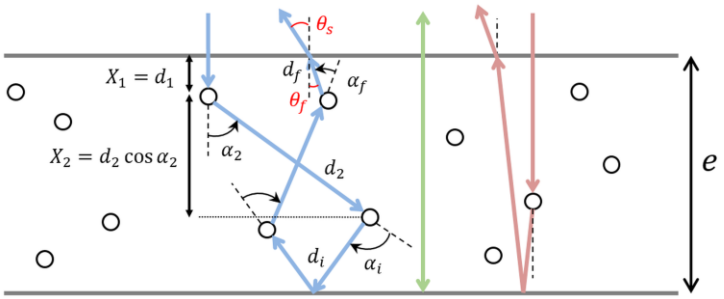

Fig. 20. Representation of the random paths of different light rays through a scattering medium of thickness e and refractive index n. The propagation can take place without diffusion (green ray), with a single diffusion (red ray) or with several diffusion phenomena (blue ray).

Once the ray has entered the medium, the distance traveled between two scattering phenomena as well as the angle with which it will be deviated, are random variables calculated from probability density functions. These densities represent the probability distributions that describe the random behavior of the variables. The random phase related to the scattering of the wave is then calculated from two variables: the distance between each scattering process and the scattering angle.

The random variable d, which defines the distance traveled by the wave until its next interaction with a scatterer, follows an exponential distribution with the rate parameter μ_{diff}. The expected value of this density is given by $1/\mu_{diff}$ and is equal to the mean free path l_{diff}. The drawing of the random variables $\{d_i\}$ is carried out using the inverse transform sampling method which consists in producing a series of random numbers following a specific distribution from the expression of its cumulative distribution function. Finally, the sequence $\{d_i\}$ is drawn using Eq. 14 where r is a random variable that follows a uniform distribution between 0 and 1.

$$d = -\frac{1}{\mu_{diff}} \ln(r); \quad r \sim U(0,1) \qquad \textbf{(14)}$$

The random variable θ, which corresponds to the scattering angle, follows a distribution P described by the Henyey-Greenstein probability density (or phase function). In order to draw the random variables $\{\theta_i\}$ according to the distribution P, the rejection sampling method is used. Briefly, the idea is to use the drawing of another random variable that is easy to simulate, to model a more complex density. Since oriented angles are used, the variable α is drawn between $-\pi$ and π. Fig. 21 shows the draw of the two random variables for different parameters.

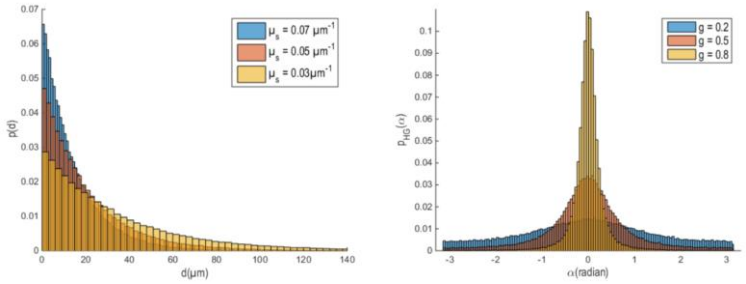

Fig. 21. Drawings of the variables d and α according to the exponential and Henyey-Greenstein laws.

The aim is to develop the interferometric signal of a structure located within the depth of a scattering layer (corresponding to the rear face of the layer of thickness e and refractive index n) (Fig. 22). The light rays reflected from the rear face may have been deflected during the crossing of the medium. They have thus traveled a greater optical distance than the "classical" optical path given by the distance of one round trip (2ne for a normal incidence). The phase shift between the reference wave and the object wave can then be determined from Figs. 20 and 22.

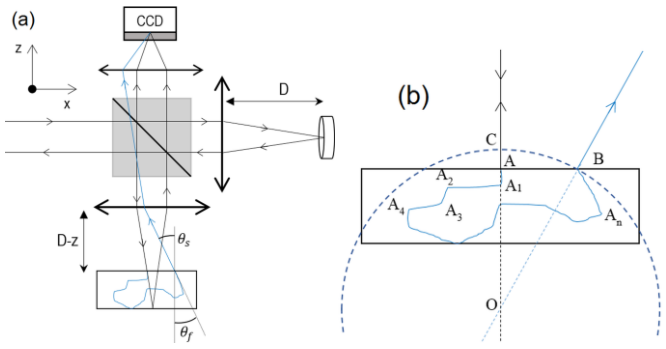

Fig. 22. (a) Path difference between a ballistic (black) and a scattered (blue) ray from the emission to the collection by the camera. (b) Phase shift at the output of the medium between a scattered ray (blue) and the reference ray (black). The reference mirror is in the plane defined by the surface of the sample.

Fig. 22 illustrates the propagation of a scattered ray compared to a ballistic ray. The random path of the scattered ray is considerably exaggerated compared to the cases of the samples usually studied (biological tissues for instance), which are generally characterized by an anisotropy factor close to 1. When leaving the layer, the scattered ray will have a random exit angle θ_s. The value of this angle directly indicates whether the ray is collected by the objective or not. In the case of collection, this exit angle may be different from the exit angle of the reference beam and leads to an additional phase shift when traveling between the sample surface and the collecting lens. From Fig. 22(b), it can be observed that the incident ray travels the same path as the reference ray until point A. It then divides at this point, and after arriving at points B and C, the object and reference rays propagate in the same way within the surrounding medium. The optical path difference between these two beams is therefore equal to:

$$\delta = [AA_1 \ldots A_n B] - [AC] = n(AA_1 + \ldots + A_n B) - (AC) \qquad \textbf{(15)}$$

Even for very inclined exit rays (θ_s close to the maximum angle of collection) and high objective NA, the distance (AC) remains negligible compared to the optical path traveled within the sample. It will be then assumed that the phase difference between the scattered wave and the reference wave is solely related to the random propagation of the beam in the scattering medium.

As explained before, the measurement of error-free backscattering spectra requires a limited effective NA, which is achieved by closing the AD. As a result, we have limited the complexity of the problem by assuming that the illumination comes down to a plane wave arriving at a normal incidence. To determine the random phase of any ray, we first perform the drawing of the random variables $\{d_i\}$. If the value of d_1 is greater than 2e (distance of one round trip in the layer for normal incidence), then the ray is not scattered. Otherwise, this means that the ray undergoes at least one scattering phenomenon during its propagation. We then draw the variables $\{\alpha_i\}$ and calculate the orthogonal projection X_i of the distance d_i along the vertical axis Z (Fig. 20). This operation is repeated as long as the ray has not emerged from the layer. The condition to fulfill for the ray to come out of the layer is as follows:

$$\sum_{?i} X_i < 0 \text{ or } \sum_i X_i > 2e \qquad \textbf{(16)}$$

with the variable X which is easily calculated further to the use of oriented angles:

$$X_i = d_i \cos\left(\sum_{u=1}^{i} a_u\right) \qquad \textbf{(17)}$$

The angle α_1 is the refraction angle after entering into the layer and is always equal to 0 for a normal incidence. X becomes negative in the case of a backscattering.

It is obviously possible for a ray to be backscattered before interacting with the rear interface or, conversely, to interact more than one time with the interface. To count the number of times the ray actually interacts with the interface, a test is performed at each scattering phenomenon (iteration). Whenever the distance travelled by the

ray along the Z-axis is smaller (respectively higher) than the sample thickness at one given iteration and that it becomes higher (respectively smaller) at the next one, it means that the ray has interacted with the rear interface. Let us suppose that Eq. 16 is achieved for i = f. The angle θ_f between the final direction of the ray and the normal to the surface is calculated from Eq. 18, where $\Sigma\alpha_i$ is returned in the range [-π, π] using Matlab's *wrapToPi* function.

$$\theta_f = \left|\sum_{i=1}^{f} \alpha_i\right| \quad \text{if} \quad \left|\sum_{i=1}^{f} \alpha_i\right| < \frac{\pi}{2}$$
$$\theta_f = \pi - \left|\sum_{i=1}^{f} \alpha_i\right| \text{otherwise} \qquad \textbf{(18)}$$

The value of the angle θ_f makes it possible to know whether the ray is refracted and then directed towards the objective, or else undergoes a total internal reflection phenomenon, in which case the ray is considered as being lost. Consequently, if the angle meets Eq. 19, the interferometric signal is simply given by the expression in Eq. 20.

$$\theta_f \geq \arcsin\left(\frac{1}{n}\right) \qquad \textbf{(19)}$$

$$I(k,z) = 2S(k)\left|r_{01}(k)\right|\cos\left(2kz + \phi_{01}\right) \qquad \textbf{(20)}$$

where $S(k)$ is still the power spectral density of the source at wave number k, $|r_{01}|$ is the amplitude reflection coefficient of the sample surface and ϕ_{01} is the phase shift due to the reflection. In the case where the ray is refracted, the exit angle θ_s is calculated using the Snell-Descartes's law.

$$\theta_s = \arcsin\left[n\sin\left(\theta_f\right)\right] \qquad \textbf{(21)}$$

If this angle is lower than the maximum angle the objective can collect, then the ray is taken into account for the calculation of the interference signal. Otherwise, the ray is lost, and the interferometric signal is as simple as Eq. 20. The maximum angle of collection is obtained from the NA of the objective:

$$\theta_{max} = \arcsin\left(NA\right) \qquad \textbf{(22)}$$

For the exact calculation of the optical path, it is necessary to sum all the distances d_i traveled by the ray before Eq. 16 is fulfilled. Of course, it is necessary to pay attention to the last value d_f that can be much larger than the distance needed for the ray to emerge from the layer. In order to determine the real distance d_f traveled by the ray before reaching the sample surface, we calculate the distance X_f, orthogonal projection of d_f over Z and satisfying Eq. 23, and subsequently recalculate d_f from Eq. 24.

$$X_f = 2e - \sum_{i=1}^{f-1} X_i \qquad \textbf{(23)}$$

$$d_f = \frac{X_f}{\cos\left(q_f\right)} \qquad \textbf{(24)}$$

The total optical path traveled by the ray is then:

$$\Delta = n\sum_{i=1}^{f} d_i \qquad \textbf{(25)}$$

We recall that the interference phenomenon can only take place within a certain area, known as the focal volume, beyond which the interference fringes are totally attenuated. It is therefore necessary to multiply each signal contributing to the formation of the final interference signal by the spatial coherence envelope of the system, which is defined by a cardinal sine function [34]. Finally, the signal corresponding to one ray collected by the objective is:

$$\begin{aligned} I\left(k,z\right) = S\left(k\right)\Bigg[& 2\left|r_{01}\left(k\right)\right|\cos\left(2kz + f_{01}\right)\left|\mathrm{sinc}\left(\frac{pzNA_{eff}^2}{2l_0}\right)\right| \\ & +2\left(1-\left|r_{01}\left(k\right)\right|^2\right)\left|r_{12}\left(k\right)\right|^p \cos\left[k\left(2z-\Delta\right)+f_{12}\right] \\ & \left|\mathrm{sinc}\left(\frac{pn\left(z-en\right)NA_{eff}^2}{2l_0}\right)\right| \end{aligned} \qquad \textbf{(26)}$$

with p the number of times the ray interacts with the rear surface. The complete construction of the interferometric signal is then performed by summing the N rays for each wavelength λ, and then adding the contribution of each wavelength in the spectrum.

$$I\left(z\right) = \sum_{k\in S}\sum_{l=1}^{N}\tilde{I}\left(k,z\right)_{(l)} \qquad \textbf{(27)}$$

where $\tilde{I}(k,z)_{(l)}$ is written either using Eq. 20 or Eq. 26 depending on the case.

2. Modeling of the interference signal in a scattering medium and validation of the model

The model developed has been applied to generating the interference signal of a 50 µm thick scattering layer for a different anisotropy factor g and different scattering coefficient μ_{diff}. The sample simulated is a layer of PDMS (polydimethylsiloxane) deposited on a silicon substrate. PDMS is a transparent material having an almost constant refractive index (~1.4) throughout the entire wavelength range considered (500-1000 nm). Silicon is an ultraviolet absorbing material whose index varies between 4 and 3.7 in the 500-1000 nm spectral range. Fig. 23 (a) shows the interferometric signal of the same layer without scattering, used as a reference. For Fig. 23 (b-e), we simulate the action of adding scatterers into the layer, which leads to the following properties:

- (b): g = 0.75 and $\mu_{diff} = 160.10^{-4}$ µm^{-1} (l_{diff} = 62.5 µm)
- (c): g = 0.75 and $\mu_{diff} = 400.10^{-4}$ µm^{-1} (l_{diff} = 25 µm)
- (d): g = 0.6 and $\mu_{diff} = 160.10^{-4}$ µm^{-1} (l_{diff} = 62.5 µm)

- (e): g = 0.2 and $\mu_{diff} = 160.10^{-4}$ μm^{-1} (l_{diff} = 62.5 µm)

The sets of parameters in (b) and (c) enable the observation of the interference signal for the cases of mean and high scattering. These values were chosen in relation to the data listed in [45] which provides the parameters g and μ_{diff} for different kinds of biological tissues. The value of g was fixed to 0.75 so that only the influence of μ_{diff} was observed. The value of 0.75 represents the average of the anisotropy factor in biological tissue, where it generally varies between 0.6 and 0.9. An attenuation in the amplitude of the rear face interferogram (PDMS-silicon interface) can be noticed as the concentration of scatterers increases. In order to study the dependency of the interferometric signal with the anisotropy factor, the scattering coefficient was set to 160.10^{-4} μm^{-1}. The signal was simulated for g = 0.6 and g = 0.2. Once again, we noticed that decreasing the anisotropy factor leads to an attenuation of the amplitude of the second interferogram.

It is worth noting that this quite simple approach makes it possible to calculate the maximum imaging depth of a scattering sample characterized from its parameters g and μ_{diff}. This maximum imaging depth is defined as that where the amplitude of the rear interface interferogram completely vanishes. If the layer studied is also subject to important absorption effects, leading to even faster attenuation, it would suffice to include the exponential decay term given by the Beer-Lambert law into the expression of I(k,z) which can be performed very easily in the program.

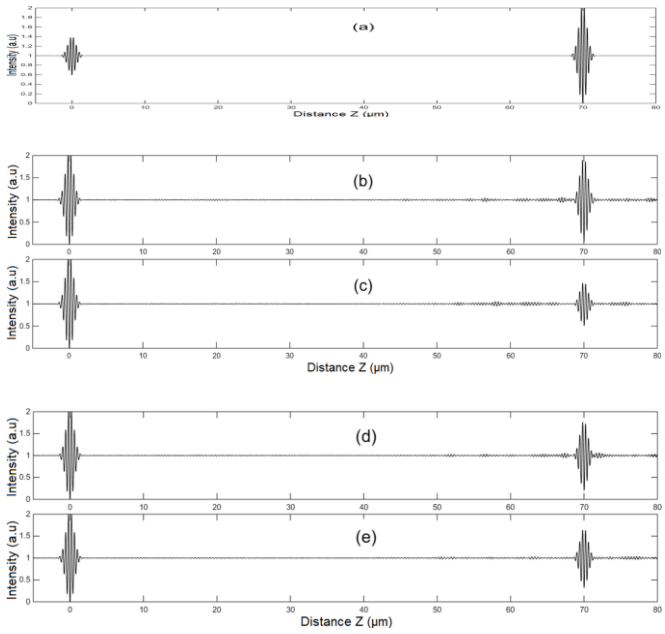

Fig. 23. (a) Simulation of the interferometric signal of the 50-µm PDMS layer without scattering. The signals are normalized with respect to the maximum intensity of the most contrasted interferogram. (b-c-d-e) Evolution of the signal of the layer for different scattering properties. (b) $\mu_{diff} = 160.10^{-4}$ μm^{-1} and g = 0.75. (c) $\mu_{diff} = 400.10^{-4}$ μm^{-1} and g = 0.75. (d) $\mu_{diff} = 160.10^{-4}$ μm^{-1} and g = 06. (e) $\mu_{diff} = 160.10^{-4}$ μm^{-1} and g = 0.2.

In order to verify the proper functioning of the program, simulations were compared to experimental measurements. The samples analyzed were manufactured within the laboratory and consist of a layer of PDMS deposited on a silicon substrate, in which particles of titanium dioxide (T_iO_2) were added at different

concentrations. These particles are often used to simulate the scattering effects occurring in biological tissues. Three layers of PDMS, each 100 µm thick, were made. The samples contain T_iO_2 particles at concentrations of 1 mg/mL, 2.5 mg/mL and 5 mg/mL respectively. Using the protocol developed in our team and in the work provided in the literature [49], the correspondence between the T_iO_2 concentration and the scattering coefficient was obtained. Regarding the factor of anisotropy, its value was not precisely calculated. However, a basic test was performed to roughly determine its order of magnitude. This test consisted in illuminating the sample at a 45° incidence and then observing the reflection and scattering of light by the sample. Indeed, the lower g is, the more the scattering spot is extended. Using a screen, two spots were observed because of the reflections on the front and back interfaces of the layer. The first spot, due to the reflection on the surface, was a one-off and very bright spot. The second spot was far more expanded, tending to indicate a relatively low value for g, but nevertheless not expanded enough to suggest a scattering close to the Rayleigh regime (g = 0). It is obvious that this test was not sufficiently accurate to give the real value of g but still enables us to estimate it to be around 0.4-06. It can be noted in the literature that methods are continuously being developed for accurately measuring the value of the anisotropy coefficient. These are mainly based on goniometric measurements [50, 51]. Experimentally, a temporal averaging of 4 images at each piezoelectric step was used for recording the interferometric images. The simulation of the interference signal of the studied scattering layer (μ_{diff} was set according to the T_iO_2 concentration) made the analysis of the PDMS-silicon interface reflectance spectrum possible. Using the same method, the spectrum was measured from the processing of the experimental signal. Both spectra are plotted in Fig. 24 and are compared to the theoretical reflectance spectrum of the interface. By using a value for g of 0.55, we found out that the three simulated spectra (red curves) matched very well with the three experimental spectra (blue curves). The high consistency between the results for each of these three different samples demonstrates the feasibility of the proposed approach for modeling an interferometric signal from a scattering layer. However, the gap between these results and the theoretical spectrum (black curve) shows that because of the scattering, it is no longer possible to perform an error-free spectral analysis.

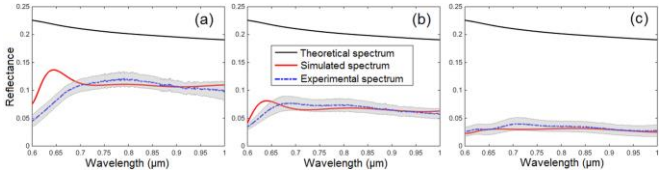

Fig. 24. Reflectance spectrum of the PDMS-silicon interface for different T_iO_2 concentrations. (a) 1mg/mL. (b) 2.5 mg/mL. (c) 5 mg/mL. The black curve represents the theoretical result, i.e. without scattering. The red curves are the results from processing simulated interference signals. The anisotropy factor is set to 0.55. The blue curves and grey areas are the experimental average results and standard deviations over 10 measurement points respectively.

2. Effect of scattering on the characterization accuracy of particles

Despite the normal incidence of the light onto the sample, it was observed that the scattering leads to an attenuation of the interference signal. This is directly related to the decrease in the number of ballistic photons and is then an inevitable phenomenon being inherent to any scattering sample. We saw that this amplitude loss leads to significant errors in the spectral analysis and could therefore subsequently prevent the process of recovering the optical and morphological properties of a particle within such media. In this section, the program developed was used and adapted to suit the case of a spherical particle immersed within the depth of a scattering layer. The anisotropy factor and the scattering coefficient were set to 0.6 and 500 cm^{-1} respectively, enabling the description of a highly scattering medium. A spherical particle with a diameter d = 5 µm and a constant refractive index n_p = 1.45 is considered. It is located at a depth of e = 40 µm within the layer whose index is assumed to be equal to that of water n = 1.33.

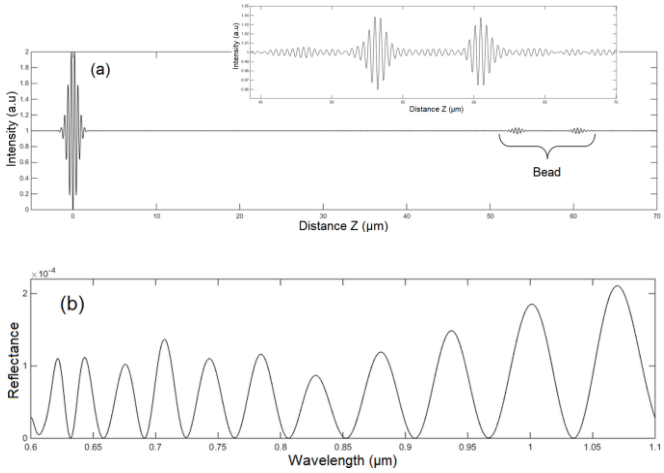

Fig. 25. (a) Simulation of the interference signal of the particle included in the scattering layer. The signal of the particle is zoomed and represented in the upper frame. (b) Backscattering spectrum of the particle.

The simulated interference signal as well as the backscattering spectrum of the buried particle is plotted in Fig. 25. In the same way as in section 4.C, the Levenberg-Marquardt algorithm and the minimization of the error function through the least squares method are used to recover the particle properties.

- Unknown refractive index and diameter

The simultaneous measurement of the index and the size of a single spherical particle through one spectral measurement is possible, as it has been demonstrated in section 4.C. Nevertheless, even in the case of a simple transparent layer, the precise determination of the index turned out to be quite difficult as it is very sensitive to any noise-induced spectrum amplitude variations. Given the significant attenuation of the backscattering spectrum oscillations, it seems very complicated, even impossible, to determine the correct refractive index of the particle. This hypothesis was verified by applying the optimization procedure to the model defined by Eq. 6.

As expected, the simulated backscattering spectrum (black curve) has a strongly attenuated amplitude compared to the theoretical spectrum (blue curve).

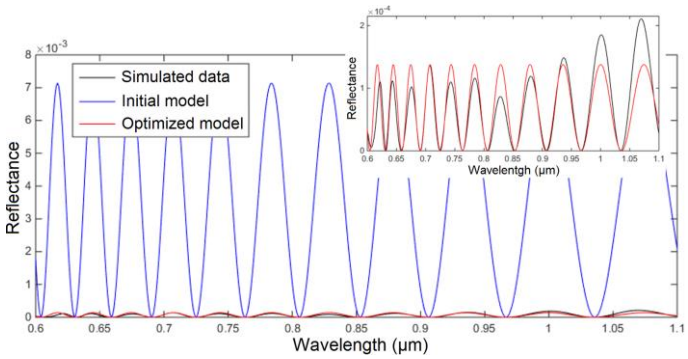

Fig. 26. Comparison between the simulated spectrum and the model defined by Eq. 6. The blue curve uses the actual diameter and optical index of the particle. The red curve uses the diameter and the index obtained from the minimization of the function χ.

Following the optimization procedure, the red spectrum is obtained and fits well to the simulated spectrum. However, the values found using the minimization of the error function are d = 5.387 µm and n_p = 1.346, which are far from d = 5 µm and n_p = 1.45. The wrong measurement of n_p further brings errors in the determination of the diameter.

- Known refractive index and unknown diameter

Nonetheless, assuming the value of the index known, the measurement of the diameter is still worth considering. Indeed, the parameter of interest for the determination of the size only lies in the frequency of the spectrum oscillations. This time, the index of the particle is set to 1.45 and the model only depends on d. Using the optimization procedure, the error function is found to be minimal for a diameter of 2.941 µm. This value does not match at all to the diameter of the particle, set to 5 µm. This difference could be explained by the large gap in amplitude between the spectra. Indeed, as it is observed in Fig. 27 (b), the error function varies between $8.6.10^{-3}$ and $9.8.10^{-3}$, resulting in an almost identical error regardless of the diameter used in the model. The minimization of this function can thus lead to an aberrant value.

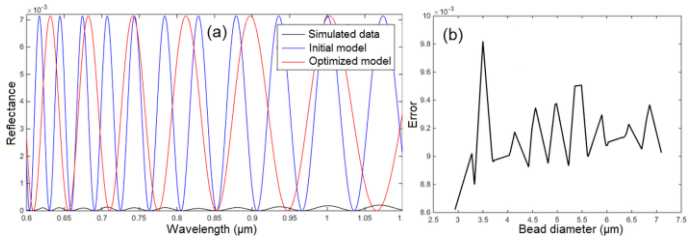

Fig. 27. (a) Comparison of the simulated spectrum with the model defined by Eq. 6. The blue curve uses the actual diameter of the particle. The red curve uses the diameter obtained from the minimization of the error function χ, which is represented in (b).

To avoid this problem, we decided to normalize each spectrum. This allows the error function to focus on the frequency of the peaks and not on their amplitude. The fact that each peak of the simulated spectrum has a random amplitude is related to the scattering of light that generates noise in the interferometric signal (Fig. 25 (a)).

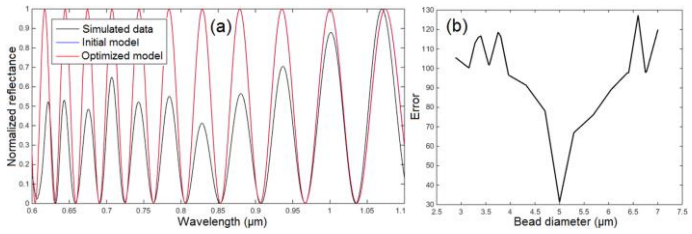

Fig. 28. (a) Comparison of the normalized simulated spectrum with the normalized model defined by Eq. 6. The blue and red curves, which respectively use the real diameter of the particle and that obtained from the minimization of the error function χ (b), are superimposed.

This time, the optimization procedure leads to a diameter of 4.998 µm. Thus, in spite of the high scattering, the diameter of the particle is accurately recovered. By knowing the value of the refractive index of the particle studied, it seems still possible to accurately measure the size of a spherical particle, even if this one is located within a scattering medium. In this case, we have seen that a normalization of both the measured and the modeling spectra was required. However, we have no doubt that the creation of a new model that would take into account the effects of scattering occurring in the sample (and absorption if required) would allow to simulate the backscattering spectrum of the bead even more precisely, and therefore to match the modeled and experimental spectra without the light scattering-induced errors. The simultaneous measurement of the size and refractive index would be still worth considering. Apart from the use of a new model, the other possible improvements, which correspond to our future work, would be to significantly reduce the noise by using, for example, a cooled camera featured by a very low noise and high quantum efficiency [52].

Conclusion

In this complete work, we have demonstrated Coherence Scanning Interferometry to be a very interesting and promising tool for the study of spherical particles. We focused on structures having a size such as the optical path is greater than the coherence length of the light source used, therefore allowing an easier post-processing and analysis. The method gathers several significant advantages whose key points are recalled hereafter. Being spatially 3D-resolved, it allows not only to detect and resolve micro and sub micro particles buried within the depth of a transparent sample, but also to discriminate them, even among high density sample, with an axial and lateral resolution of about 0.8 µm and 2.8 µm respectively. While not being its first benefit, the method does not require excessive long acquisition times since only one scanning along Z is operated with a duration that depends on the thickness of the sample. Thanks to the one-point measurement feature of interference

microscopy and digital signal processing, our method is then very fast and only takes a few seconds. Its best asset lies in the ability of recovering quantitative information about these structures with a good accuracy. As a matter of fact, we have demonstrated the possibility of extracting simultaneously the diameter and the refractive index of beads, without any prior knowledge on their features. Despite using a simplified backscattering model and the very low index contrast between the beads and the surrounding medium (0.1 for polystyrene beads and 0.03 in the case of silica) resulting in a rather weak quality of the interference signals, the results are satisfactory in terms of precision with the determination of the size of the beads being very often conclusive. However, we have shown an important correlation between the measurement accuracy of the refractive index and the signal-to-noise ratio that may result, in some cases, to a wrong interpretation of the recovered spectrum and lead to aberrant values of the bead properties. The proposed method has been extended for analyzing structures contained in scattering media and its performances studied theoretically. In this particular case, we demonstrated that the use of our simplified backscattering spectrum model only allows the recovery of the particle size assuming its refractive index to be already known. With the further improvements suggested, we nonetheless think that this method could be used for disease detection in a complex biological environment as it would enable the identification of structures based on both their size and optical index whose modification is often an indication of health issues.

Acknowledgments. The authors would like to acknowledge the financial support of this work from the University of Strasbourg and INSA Strasbourg. The authors also wish to thank Stéphane Roques, Nicolas Zimmerman and Thomas Regrettier as well as the staff from the C^3FAB platform for the sample preparation.

REFERENCES

[1] M. J. T. Stubbington, O. Rozenblatt-Rosen, A. Regev, S. A. Teichmann, Single-cell transcriptomics to explore the immune system in health and disease, *Science.* 358 (2017) 58-63. https://doi.org/10.1126/science.aan6828.

[2] M. Shan, M. E. Kandel, G. Popescu, Refractive index variance of cells and tissues measured by quantitative phase imaging, Opt. Express. 25 (2017) 1573-1581. https://doi.org/10.1364/OE.25.001573.

[3] C. Balas, G. Epitropou, A. Tsapras, N. Hadjinicolaou, Hyperspectral imaging and spectral classification for pigment identification and mapping in paintings by El Greco and his workshop, Multimedia Tools and Applications. 77 (2018) 9737-9751. https://doi.org/10.1007/s11042-017-5564-2.

[4] D. Kwon, V. W. Or, M. J. Sovers, M. Tang, P. D. Kleiber, V. H. Grassian, M. A. Young, Optical Property Measurements and Single Particle Analysis of Secondary Organic Aerosol Produced from the Aqueous-Phase Reaction of Ammonium Sulfate with Methylglyoxal, *ACS Earth Space Chem.* 2 (2018) 356-365. 10.1021/acsearthspacechem.8b00004.

[5] S. J. Sahl, S. W. Hell, S. Jakobs, Fluorescence nanoscopy in cell biology, Nature Reviews Molecular Cell Biology, 18 (2017) 685–701. https://doi.org/10.1038/nrm.2017.71.

[6] S. J. Leavesley, N. Annamdevula, J. Boni, S. Stocker, K. Grant, B. Troyanovsky, T. C. Rich, D. F. Alvarez, HyperSpectral imaging microscopy for identification and quantitative analysis of fluorescently-labeled cells in highly autofluorescent tissue, J. Biophotonics. 5 (2012) 67–84. https://doi.org/10.1002/jbio.201100066.

[7] F. Huth, A. Govyadinov, S. Amarie, W. Nuansing, F. Keilmann, R. Hillenbrand, Nano-FTIR Absorption Spectroscopy of Molecular Fingerprints at 20 nm Spatial Resolution, Nano Lett. 12 (2012) 3973–3978. https://doi.org/10.1021/nl301159v.

[8] Amenabar, S. Poly, W. Nuansing, E. H. Hubrich, A. A. Govyadinov, F. Huth, R. Krutokhvostov, L. Zhang, M. Knez, J. Heberle, A. M. Bittner, R. Hillenbrand, Structural analysis and mapping of individual protein complexes by infrared nanospectroscopy, Nat. Commun. 4 (2013) 2890. https://doi.org/10.1038/ncomms3890.

[9] M. Brehm, T. Taubner, R. Hillenbrand, F. Keilmann, Infrared Spectroscopic Mapping of Single Nanoparticles and Viruses at Nanoscale Resolution, Nano Lett. 6 (2006) 1307–1310. https://doi.org/10.1021/nl0610836.

[10] S. Patskovsky, E. Bergeron, M. Meunier, Hyperspectral darkfield microscopy of PEGylated gold nanoparticles targeting CD44-expressing cancer cells, J. Biophotonics. 8 (2013) 162–167. https://doi.org/10.1002/jbio.201300165.

[11] S. Patskovsky, E. Bergeron, D. Rioux, M. Meunier, Wide-field hyperspectral 3D imaging of functionalized gold nanoparticles targeting cancer cells by reflected light microscopy, J. Biophotonics. 8 (2015) 401–407. https://doi.org/10.1002/jbio.201400025.

[12] R. Badireddy, M. R. Wiesner, J. Liu, Detection, Characterization, and Abundance of Engineered Nanoparticles in Complex Waters by Hyperspectral Imagery with Enhanced Darkfield Microscopy, Environ. Sci. Technol. 46 (2012) 10081–10088. https://doi.org/10.1021/es204140s

[13] S. Patskovsky, E. Bergeron, D. Rioux, M. Simard, M. Meunier, Hyperspectral reflected light microscopy of plasmonic Au/Ag alloy nanoparticles incubated as multiplex chromatic biomarkers with cancer cells, Analyst. 139 (2014) 5247–5253. https://doi.org/10.1039/C4AN01063A.

[14] Y. Liu, X. Li, Y. L. Kim, V. Backman, Elastic backscattering spectroscopic microscopy, Opt. Lett. 30 (2005) 2445–2447. https://doi.org/10.1364/OL.30.002445.

[15] A. Wax, C. Yang, R. R. Dasari, M. S. Feld, Measurement of angular distributions by use of low-coherence interferometry for light-scattering spectroscopy, Opt. Lett. 26 (2001) 322–324. https://doi.org/10.1364/OL.26.000322.

[16] J. W. Pyhtila, R. N. Graf, A. Wax, Determining nuclear morphology using an improved angle-resolved low coherence interferometry system, Opt. Express. 11 (2003) 3473–3484. https://doi.org/10.1364/OE.11.003473.

[17] J. W. Pyhtila, J. D. Boyer, K. J. Chalut, A. Wax, Fourier-domain angle-resolved low coherence interferometry through an endoscopic fiber bundle for light-scattering spectroscopy, Opt. Lett. 31 (2006) 772–774. https://doi.org/10.1364/OL.31.000772.

[18] C. L. Bennett, M. R. Carter, D. J. Fields, J. A. Moreno-Hernandez, Imaging Fourier transform spectrometer, Proceedings of SPIE. 1937 (1993) 191-200. https://doi.org/10.1117/12.157065

[19] C. Dorrer, N. Belabas, J-P. Likforman, M. Joffre, Spectral resolution and sampling issues in Fourier transform spectral interferometry, 17 (2000) 1795-1802. https://10.1364/JOSAB.17.001795

[20] P. Montgomery, D. Montaner, O. Manzardo, M. Flury, H-P. Herzig, The metrology of a miniature FT spectrometer MOEMS device using white light scanning interference microscopy, Thin Solid Films. 450 (2004) 79–83. http://doi.org/10.1016/j.tsf.2003.10.055.

[21] A. Dubois, L. Vabre, A-C. Boccara, E. Beaurepaire, High-Resolution Full-Field Optical Coherence Tomography with a Linnik Microscope, Appl. Opt. 41 (2002) 805-812. https://doi.org/10.1364/AO.41.000805.

[22] R. Claveau, P. Montgomery, M. Flury, D. Montaner, Local reflectance spectra measurements of surfaces using coherence scanning interferometry, Proceeding of SPIE. 9890 (2016) 98900Q-1. https://doi.org/10.1117/12.2227625.

[23] A. Morin, J-M. Frigerio, Aperture effect correction in spectroscopic full-field optical coherence tomography, App. Opt. 51 (2012) 3431-3438. https://doi.org/10.1364/AO.51.003431

[24] R. Claveau, P. Montgomery, M. Flury, Application of coherence scanning interferometry for local spectral characterization of transparent layers", Proceeding of SPIE. 10678 (2018) 10678L-1. https://doi.org/10.1117/12.2314921.

[25] R. Claveau, P. Montgomery, M. Flury, D. Montaner, Depth-resolved local reflectance spectra measurements in full-field optical coherence tomography," Opt. Express. 25 (2017) 20216-20232. https://doi.org/10.1364/OE.25.020216.

[26] K. B. Thovsen, Evaluation of Mie scatter approximation formulas for the scattering of infrared light at biological cells, Master Thesis, Norwegian University of Life Sciences (2013).

[27] B. Mätzler, MATLAB functions for Mie scattering and absorption version 2, Research Report, Institut für Angewandte Physik, Bern University, 2002, pp. 1-24.

[28] W. J. Wiscombe, Improved Mie scattering algorithms, Appl. Opt. 19 (1980) 1505–1509. https://doi.org/10.1364/AO.19.001505.

[29] A. Deirmendjian, Tables of Mie scattering cross sections and amplitudes, Santa Monica, CA: RAND Corporation, 1963, pp. 1-46.

[30] M. Born, E. Wolf, Partially coherent light, in Principles of Optics, Cambridge University Press, 1999, pp. 595–599.

[31] M. Fauver, E. Seibel, J. R. Rahn, M. Meyer, F. Patten, T. Neumann, A. Nelson, Three-dimensional imaging of single isolated cell nuclei using optical projection tomography, Opt. Express. 13 (2005) 4210–4223. https://doi.org/10.1364/OPEX.13.004210.

[32] J. Kirschner, On the influence of backscattered electrons on the lateral resolution in scanning auger microscopy, Appl. Phys. 14 (1977) 351–354. https://doi.org/10.1007/BF00883438.

[33] A. Dubois, K. Grieve, G. Moneron, R. Lecaque, L. Vabre, C. Boccara, Ultrahigh-Resolution Full-Field Optical Coherence Tomography, Appl. Opt. 43 (2004) 2874-2883. https://doi.org/10.1364/AO.43.002874.

[34] I. Zeylikovich, Short coherence length produced by a spatial incoherent source applied for the Linnik-type interferometer, Appl. Opt. 47 (2008) 2171-2177 (2008). https://doi.org/10.1364/AO.47.002171.

[35] S. W. Kim, G. H. Kim, Thickness-profile measurement of transparent thin-film layers by white-light scanning interferometry, Appl. Opt. 38 (1999) 5968–5973. https://doi.org/10.1364/AO.38.005968.

[36] S. K. Debnath, M. P. Kothiyal, J. Schmit, P. Hariharan, Spectrally resolved white-light phase-shifting interference microscopy for thickness-profile measurements of transparent thin film layers on patterned substrates, Opt. Express. 14 (2006) 4662-4667. https://doi.org/10.1364/OE.14.004662.

[37] D. S. Wan, Measurements of thin films using fourier amplitude, US Patent 7612891 B2 (2009).

[38] J. Dong, R. Lu, Sensitivity analysis of thin-film thickness measurement by vertical scanning white-light interferometry, Appl. Opt. 51 (2012) 5668–5675. https://doi.org/10.1364/AO.51.005668.

[39] T. Guo, J. Wu, L. Ni, X. Fu, X. Hu, Initial estimation of thin film thickness measurement based on white light spectral interferometry, Thin Solid Films. 612 (2016) 267–273. https://doi.org/10.1016/j.tsf.2016.06.025.

[40] T. Jo, K. Kim, S. Kim, H. Pahk, Thickness and Surface Measurement of Transparent Thin-Film Layers using White Light Scanning Interferometry Combined with Reflectometry, J. Opt. Soc. Korea. 18 (2014) 236–243. https://doi.org/10.3807/JOSK.2014.18.3.236.

[41] R. Claveau, P. Mongomery, M. Flury, G. Ferblantier, Local inspection of refractive index and thickness of thick transparent layers using spectral reflectance measurements in low coherence

scanning interferometry, Opt. Materials. 86 (2018) 100-105. https://doi.org/10.1016/j.optmat.2018.09.046.

[42] A. Leong-Hoi, R. Claveau, M. Flury, W. Uhring, B. Serio, F. Anstotz, P. Montgomery, Detection of defects in a transparent polymer with high resolution tomography using white light scanning interferometry and noise reduction, Proceeding of SPIE, 9528 (2015) 952807. https://doi.org/10.1117/12.2184559.

[43] N. Sultanova, S. Kasarova, I. Nikolov, Dispersion Properties of Optical Polymers, Acta Phys. Polonica A. 116 (2009) 585-587. https://doi.org/10.12693/APhysPolA.116.585.

[44] H. Malitson, Interspecimen Comparison of the Refractive Index of Fused Silica, J. Opt. Soc. Am. 55 (1965) 1205-1209**.** https://doi.org/10.1364/JOSA.55.001205.

[45] N. Bashkatov, E. A. Genina, V. V. Tuchin, Optical properties of skin, subcutaneous, and muscle tissues: a review, J. Innov. Opt. Health Sci. 04 (2011) 9–38. https://doi.org/10.1142/S1793545811001319.

[46] L. O. Reynolds, N. J. McCormick, Approximate two-parameter phase function for light scattering, J. Opt. Soc. Am. 70 (1980) 1206–1212. https://doi.org/10.1364/JOSA.70.001206.

[47] W. M. Cornette, J. G. Shanks, Physically reasonable analytic expression for the single-scattering phase function, Appl. Opt. 31 (1992) 3152–3160. https://doi.org/10.1364/AO.31.003152.

[48] D. Toublanc, Henyey–Greenstein and Mie phase functions in Monte Carlo radiative transfer computations, Appl. Opt. 35 (1996) 3270–3274. https://doi.org/10.1364/AO.35.003270.

[49] F. Ayers, A. Grant, D. Kuo, D. J. Cuccia, A. J. Durkin, Fabrication and characterization of silicone-based tissue phantoms with tunable optical properties in the visible and near infrared domain, Proceeding of SPIE. 6870 (2008) 687007–687009. https://doi.org/10.1117/12.764969.

[50] M. L. Askoura, F. Vaudelle, J.-P. L'Huillier, Multispectral measurement of scattering-angular light distribution in apple skin and flesh samples, Appl. Opt. 55 (2016) 9217 (2016). https://doi.org/10.1364/AO.55.009217.

[51] G. Hall, S. L. Jacques, K. W. Eliceiri, P. J. Campagnola, Goniometric measurements of thick tissue using Monte Carlo simulations to obtain the single scattering anisotropy coefficient, Biomed. Opt. Express. 3 (2012) 2707–2719. https://doi.org/10.1364/BOE.3.002707.

[52] P. C. Montgomery, F. Anstotz, F. Salzenstein, D. Montaner, Real time and high quality on-line 4D FF-OCT using continuous fringe scanning with a high-speed camera and FPGA image processing, in: A. Dubois (Ed.), Full-Field Optical Coherence Microscopy: technology and applications, Pan Stanford Publishing, Singapore, 2016. Pp. 393-428. https://doi.org/10.4032/9789814669177.